RSC Advances

PAPER

View Article Online
View Journal | View Issue

Cite this: *RSC Adv.*, 2026, **16**, 27884

Development of new quinoline-triazole based hybrids: synthesis, nano-encapsulation, DFT calculations, and evaluation of antidiabetic and antioxidant activity

Fatma M. Elhalmoushy, [a] Mohamed N. Abd Al Moaty, [ab] Alaa S. Hegazy, [c] Saied M. Soliman, [a] Mazen Sherif, [d] Doaa A. Ghareeb, [def] Mohamed Hagar *[a] and Manar Ahmed Fouad *[a]

Currently, the development of effective and safe antidiabetic drugs remains a major challenge in diabetes management. This study reports the design and synthesis of new quinoline-based hybrids, featuring an oxymethylene-linked 1,2,3-triazole core and integrated 1,2,4-triazole pharmacophores, alongside their chitosan-encapsulated derivatives, as prospective multitarget antidiabetic agents. The synthesized compounds were evaluated for their *in vitro* inhibitory activity against α-amylase and α-glucosidase, as well as for glucose uptake stimulation and their antioxidant potential through NO and DPPH radical scavenging assays. Notably, **CNPs 5*** and **6*** demonstrated significant α-amylase and α-glucosidase inhibitory potencies, surpassing that of the standard drug acarbose. Compound **6*** (IC_{50} = 0.17 μM) exhibited the most potent α-amylase inhibition compared to acarbose (IC_{50} = 25.08 μM), alongside demonstrating significant NO radical scavenging activity with a potency ~1.78-fold greater than ascorbic acid. Furthermore, it stimulated glucose uptake at a level ~1.65-fold higher than Berberine. **CNPs 5*** (IC_{50} = 58.21 μM) was identified as the most potent α-glucosidase inhibitor, surpassing acarbose (IC_{50} = 68.91 μM). To elucidate the electronic properties and stability of the new hybrids, DFT calculations were performed. Subsequently, molecular docking studies were conducted to corroborate the *in vitro* findings and explore the binding interactions within the active sites of the target enzymes. Finally, ADME profiles of the new hybrids suggest their promising drug-like properties and support further investigation as potential antidiabetic leads.

Received 12th February 2026
Accepted 18th May 2026

DOI: 10.1039/d6ra01266c

rsc.li/rsc-advances

1. Introduction

Type 2 diabetes mellitus (T2DM) presents a significant and growing challenge to global health. In 2014, the World Health Organization reported 422 million people living with this condition worldwide, a number that has risen sharply.[1] By 2021, the International Diabetes Federation (IDF) estimated the global prevalence among adults had reached >10%, or approximately 536.6 million individuals, with projections suggesting it will climb to >12%, affecting more than 783 million people, by 2045.[2,3] This trajectory underscores the escalating scale of a disease characterized primarily by insulin resistance, a condition affecting an estimated 95% of patients that disrupts blood glucose regulation and significantly heightens the risk of devastating complications, including heart disease, stroke, and kidney failure.[4,5] Managing postprandial blood glucose spikes through the inhibition of key digestive enzymes, such as α-amylase and α-glucosidase, represents a crucial therapeutic strategy, mirroring the mechanism of drugs like acarbose.[6,7] However, currently available drugs are often limited by adverse side effects and inadequate long-term efficacy, highlighting the urgent need for safer and more potent therapeutic alternatives.[8]

In this context, medicinal chemistry offers a promising avenue for the development of new antidiabetic agents. In this pursuit, N-heterocyclic compounds have been invaluable for decades, forming the backbone of numerous therapeutic agents, owing to their remarkable structural versatility and

[a]*Department of Chemistry, Faculty of Science, Alexandria University, P.O. Box 426, Alexandria 21321, Egypt. E-mail: mohamed.hagar@alexu.edu.eg; manar.ahmed@alexu.edu.eg*

[b]*Chemistry Department, Faculty of Advanced Basic Science, Alamein International University, Alamein City, Matrouh Governorate, Egypt*

[c]*Department of Medical Laboratory Technology, Faculty of Applied Health Sciences Technology, Pharos University in Alexandria, Alexandria, Egypt*

[d]*Bio-screening and Preclinical Trial Lab, Biochemistry Department, Faculty of Science, Alexandria University, Alexandria, Egypt*

[e]*Center of Excellence for Drug Preclinical Studies (CE-DPS), Pharmaceutical and Fermentation Industry Development Center, City of Scientific Research & Technological Applications (SRTA-city), New Borg El Arab, Alexandria, Egypt*

[f]*Research Projects Unit, Pharos University in Alexandria, Canal El Mahmoudia Street, Beside Green Plaza Complex, 21648, Alexandria, Egypt*

broad biological relevance.[9–13] Within this important class, quinoline derivatives emerge as a highly promising scaffold. Quinolines are particularly noteworthy for their broad spectrum of biological activities, including anticancer,[14] antimalarial,[15] antiviral,[16] anti-inflammatory,[17] anti-leishmanial,[18] and notably, antidiabetic effects.[19] Their proven utility is further highlighted by the fact that several successful antibiotic drugs, such as ciprofloxacin, norfloxacin, and ofloxacin, belong to this family (Fig. 1). This well-established pharmacological profile makes the quinoline scaffold a rational starting point for the design of new antidiabetic candidates.

In parallel to the quinoline scaffold, the triazole ring holds great promise for drug design. The triazole ring system, encompassing 1,2,3-triazole and 1,2,4-triazole isomers, is recognized as a privileged pharmacophore in modern drug discovery, featuring prominently in numerous bioactive molecules with diverse therapeutic applications.[20,21] The 1,2,3-triazole is especially important because it can be efficiently constructed *via* the Nobel Prize-winning "Click" reaction. This reliable and high-yielding method provides a modular way to link different pharmacophores together.[22] This ability makes the 1,2,3-triazole an excellent chemical bridge, enabling the powerful strategy of molecular hybridization. By connecting a quinoline unit to another active fragment through this triazole linker, chemists can efficiently create new hybrid molecules. The goal is to combine the beneficial properties of both components, potentially yielding hybrid compounds with enhanced potency and improved interactions with antidiabetic molecular targets.[23]

While molecular potency is essential, therapeutic efficacy also depends on adequate drug delivery and bioavailability. Here, nanotechnology offers a significant advantage. Reducing a drug's particle size to the nanoscale can greatly improve its water solubility, bioavailability, and overall efficacy, which is why nanoparticles are a major focus of recent clinical investigations.[24] These particles are well-established in drug development, playing key roles in therapies for infectious diseases and cancer, with growing applications in diabetes research.[25] Among the various types, polymeric nanoparticles are particularly promising due to their excellent biocompatibility and controllable properties.[26] In the last decade, polymeric chitosan nanoparticles have gained considerable attention. Chitosan is a natural, biodegradable biopolymer derived from chitin, recognized by the FDA as Generally Recognized As Safe (GRAS), with favorable biocompatibility and non-allergenic properties that make it a well suited carrier for oral drug delivery formulations.[27] Therefore, pairing the potential bioactive hybrids with chitosan-based nanoparticles could be a cohesive strategy to enhance their potential as an antidiabetic agent, simultaneously optimizing molecular bioactivity and systemic bioavailability.

Therefore, herein we report the synthesis of new hybrids that integrate 1,2,4-triazole and 1,2,3-triazole moieties with a quinoline backbone, along with their corresponding chitosan-encapsulated formulations. This work aims to develop more potent multitargeted antidiabetic agents with a potentially reduced risk of adverse effects. The synthesized compounds were evaluated for their antidiabetic potential, including *in vitro* dual–inhibitory activity against α-amylase and α-glucosidase enzymes and their ability to enhance glucose uptake in yeast cells. Given the established link between oxidative stress and the pathogenesis of diabetic complications,[28] their antioxidant activity against diphenyl-1-picrylhydrazyl (DPPH) and nitric oxide (NO) was also investigated. To understand the molecular basis of their activity, chemoinformatic studies were performed, including molecular docking simulations to identify key interactions within the target enzymes' active sites. Density functional theory (DFT) calculations were introduced to elucidate the electronic properties and stability of the new hybrids. Finally, ADME (Absorption, Distribution, Metabolism, and Excretion) profiles were assessed to evaluate the compounds' potential for further preclinical development.

2. Design rationale

The design of the new hybrids was inspired by previously reported antidiabetic agents (Fig. 2).[8,20,29,30] The key pharmacophoric features incorporated into the target structures include: (i) quinoline and triazole moieties as the core N-heterocyclic scaffolds; (ii) a flexible methylene linker to provide rotational freedom; (iii) an imine group (–C=N–) capable of engaging both electrophilic and nucleophilic residues within enzyme active sites;[31] and (iv) an aryl group to impart favorable lipophilic character. To complement this molecular design, the synthesized hybrids were subsequently encapsulated within chitosan nanoparticles to enhance solubility and bioavailability.

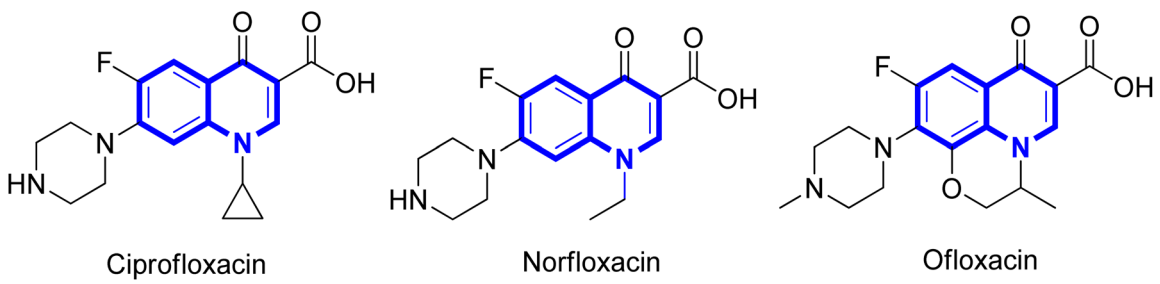

Fig. 1 Structures of quinoline-based antibiotics.

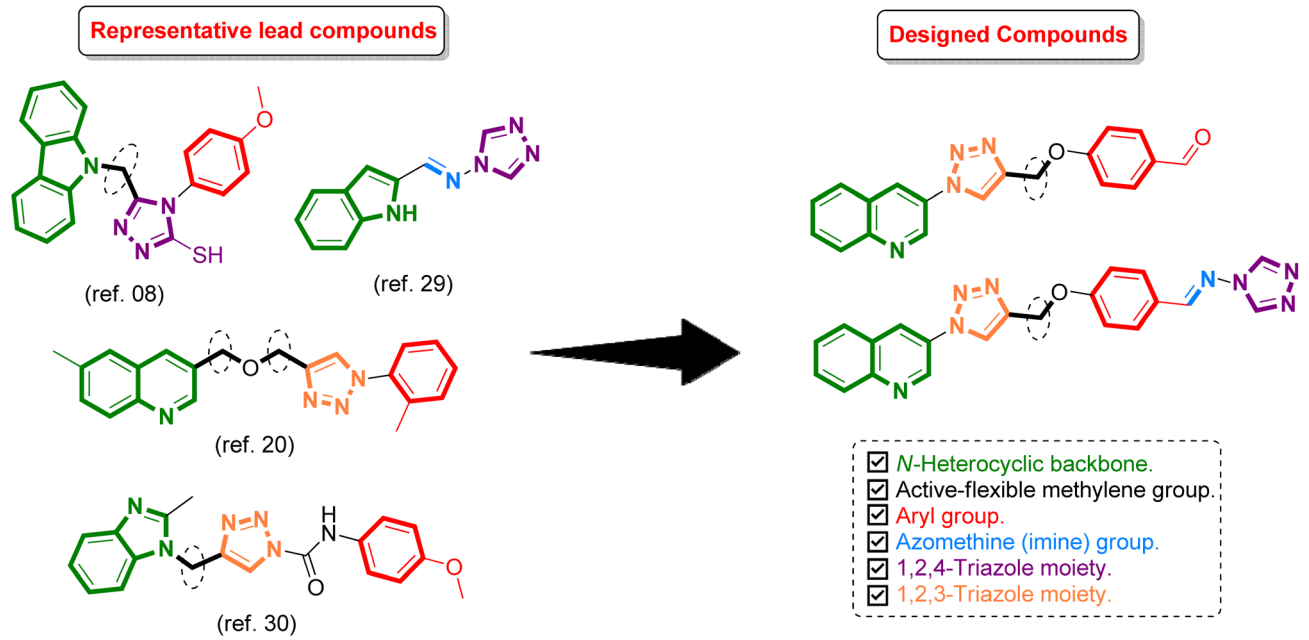

Fig. 2 Rationale design and key pharmacophoric features of the target hybrids.

3. Results and discussion

3.1. Chemistry

In this work we aimed to construct a new molecular hybrid architecture by linking 3-azidoquinoline **2** and 4-(prop-2-yn-1-yloxy)benzaldehyde **4** moieties *via* click chemistry. This Cu(I)-catalyzed 1,3-dipolar cycloaddition (CuAAC) 'Click' reaction established a central 1,2,3-triazole ring, providing the key aldehyde-functionalized scaffold **5**. The resulting aldehyde **5** was then subjected to an imination reaction with a primary aromatic amine to yield the corresponding Schiff base **6** which features both 1,2,3- and 1,2,4- triazole motifs, as shown in Scheme 1.

The previously reported compounds **2** and **4** were resynthesized in the present study as the foundational precursors for the preparation of the targeted compound **5**. Thus, 3-aminoquinoline was converted to 3-azidoquinoline **2** *via* an aromatic nucleophilic substitution reaction proceeding through a diazonium salt intermediate, affording the desired product in an excellent yield (98%) according to a reported procedure (Scheme 1A).[32] In parallel, 4-(prop-2-yn-1-yloxy)benzaldehyde **4** was obtained by propargylation of 4-hydroxybenzaldehyde **3** using

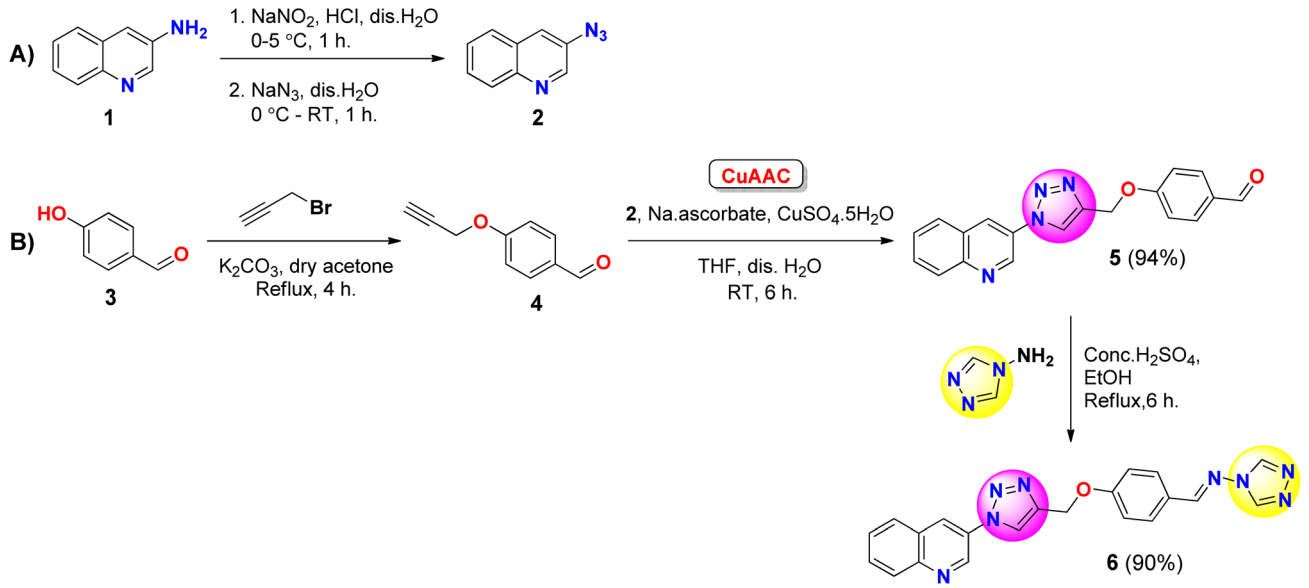

Scheme 1 Synthesis of new quinoline-based hybrids incorporating 1,2,3-triazole **5** and 1,2,4-triazole moieties **6**.

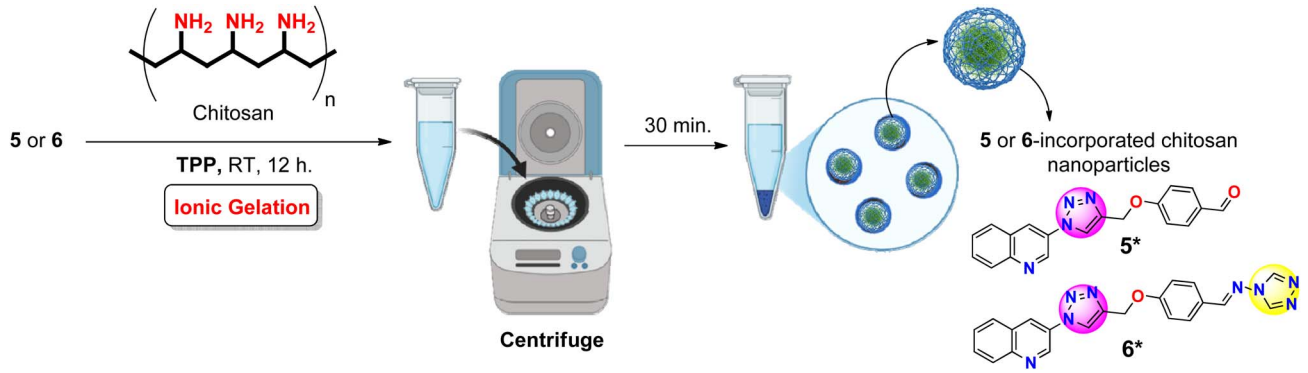

Scheme 2 Synthesis of chitosan nanoparticles loaded with **5** or **6** *via* ionic gelation.

propargyl bromide. Subsequent CuAAC between azide **2** and alkyne **4** afforded the key aldehyde, 4-((1-(quinolin-3-yl)-1*H*-1,2,3-triazol-4-yl)methoxy)benzaldehyde **5**, in 94% yield (Scheme 1B).

The structure of **5** was confirmed by its IR spectrum, which showed characteristic absorption bands for the triazole ring (Csp^2-H stretching at 3138 cm^{-1}), the methylene group (asymmetric CH_2 stretch at 2923 cm^{-1} and symmetric CH_2 stretch at

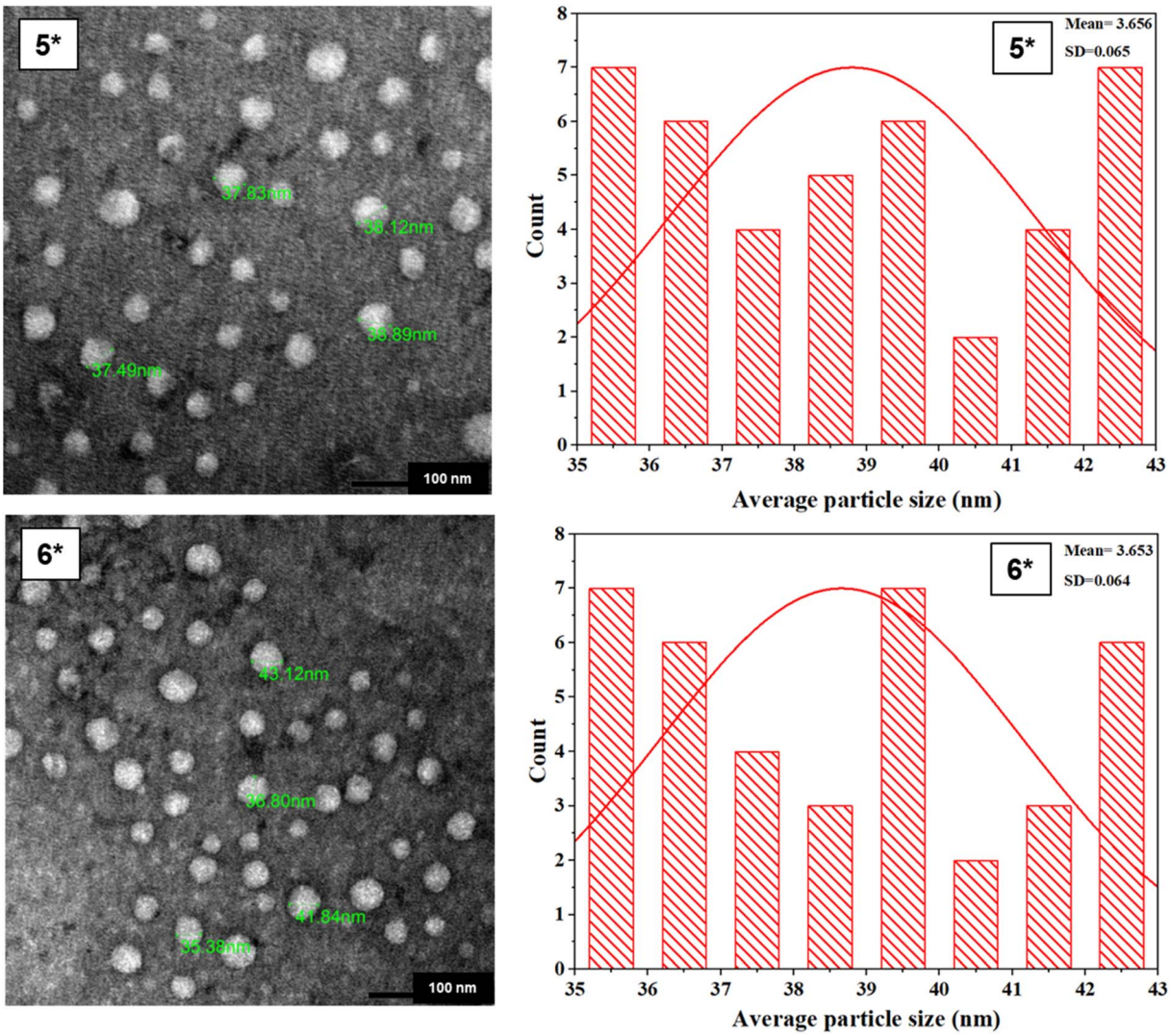

Fig. 3 TEM images (magnification: 50 000×; scale bars: 100 nm) and corresponding particle size distribution histograms of CNPs **5*** and **6***.

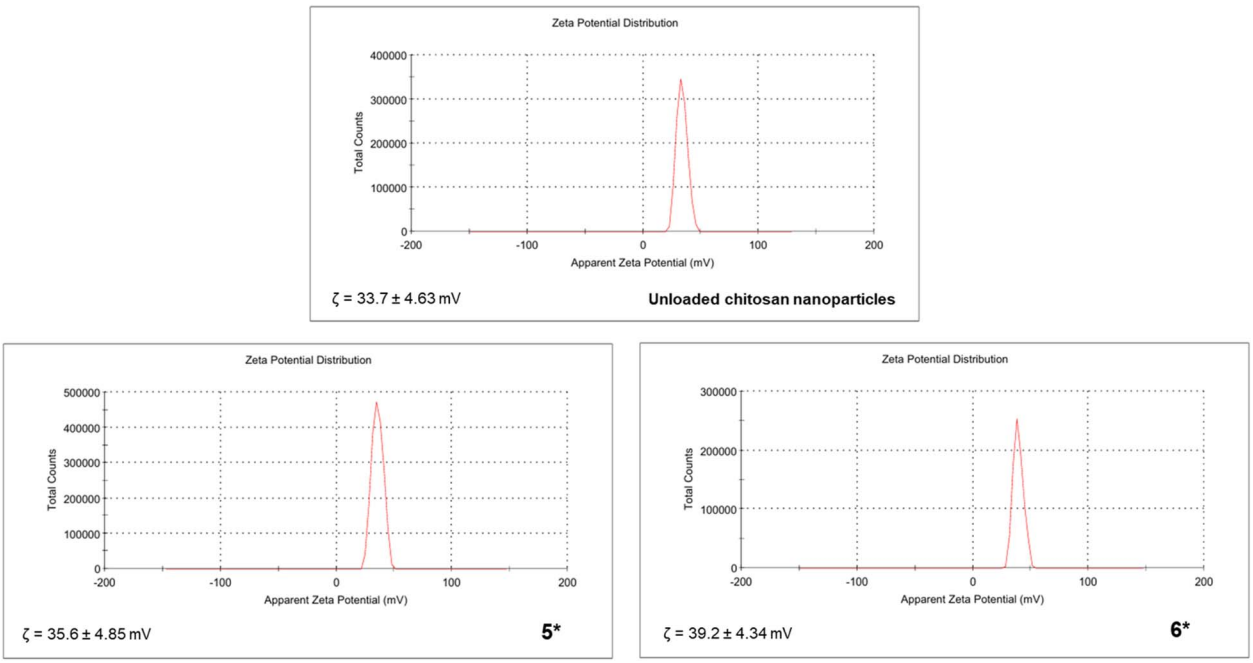

Fig. 4 Zeta potential distribution curves of unloaded chitosan nanoparticles, **5*** and **6***. Measurements were performed in distilled water (ionic strength ~10^{-7} M, zeta values represented as mean ± SD, $n = 3$).

Table 1 EE% and DL% values of **CNPs 5*** and **6***

Nanoformulation	EE% (mean ± SD)[a]	DL% (mean ± SD)[a,b]
CNPs 5*	99.59 ± 0.15	9.1 ± 0.10
CNPs 6*	99.93 ± 0.21	9.3 ± 0.13

[a] Values are expressed as mean ± SD, $n = 3$, no significant difference between formulations ($p > 0.05$). [b] Theoretical maximum DL% = 9.09%, calculated based on the initial drug-to-chitosan mass ratio (1 : 10 w/w).

2840 cm^{-1}), and the aldehyde group (C═O stretch at 1686 cm^{-1}). Moreover, ^{1}HNMR spectrum displayed characteristic peaks for the aldehyde proton at 9.89 ppm, a singlet at δ 9.21 ppm corresponding to H-5 proton of the 1,2,3-triazole ring, and a singlet at δ 5.45 ppm for the methylene group protons (–C**H**$_2$–). In the ^{13}C NMR spectrum, a signal was observed at δ 191.5 ppm corresponding to the carbonyl carbon and another signal at δ 61.4 ppm corresponding to the methylene carbon (–**C**H$_2$–).

To introduce the 1,2,4-triazole moiety and complete the target molecular architecture, aldehyde **5** was subjected to an acid catalyzed imination reaction with 4-amino-1,2,4-triazole. This condensation afforded Schiff base (*E*)-*N*-(4-((1-(quinolin-3-yl)-1*H*-1,2,3-triazol-4-yl)methoxy)benzylidene)-4*H*-1,2,4-triazol-4-amine **6** in 90% yield. The IR spectrum of **6** showed characteristic absorption bands for the triazole ring (Csp^2-H stretching at 3105 cm^{-1}), the methylene group (asymmetric CH_2 stretch at 2935 cm^{-1} and symmetric CH_2 stretch at 2851 cm^{-1}), and a (C═N stretch at 1613 cm^{-1}). The structure was further confirmed by ^{1}HNMR, which showed the disappearance of the aldehyde proton in compound **5** and the appearance of the singlet imine proton (**H**C═N) at δ 9.03 ppm in addition to the two protons of the 1,2,4-triazole ring at δ 9.18 ppm. Key signals remaining from **5** included the H-5 proton of the 1,2,3-triazole ring at δ 9.21 ppm and the methylene group (-C**H**$_2$-) protons as a singlet at δ 5.42 ppm. In the ^{13}CNMR, disappearance of the carbonyl signal and appearance of imine carbon at δ 161.2 ppm confirmed the formation of the target imine.

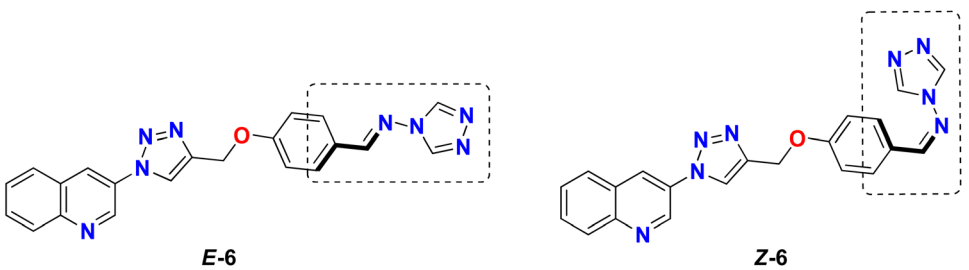

Fig. 5 (*E*)- and (*Z*)-isomers of compound**6**.

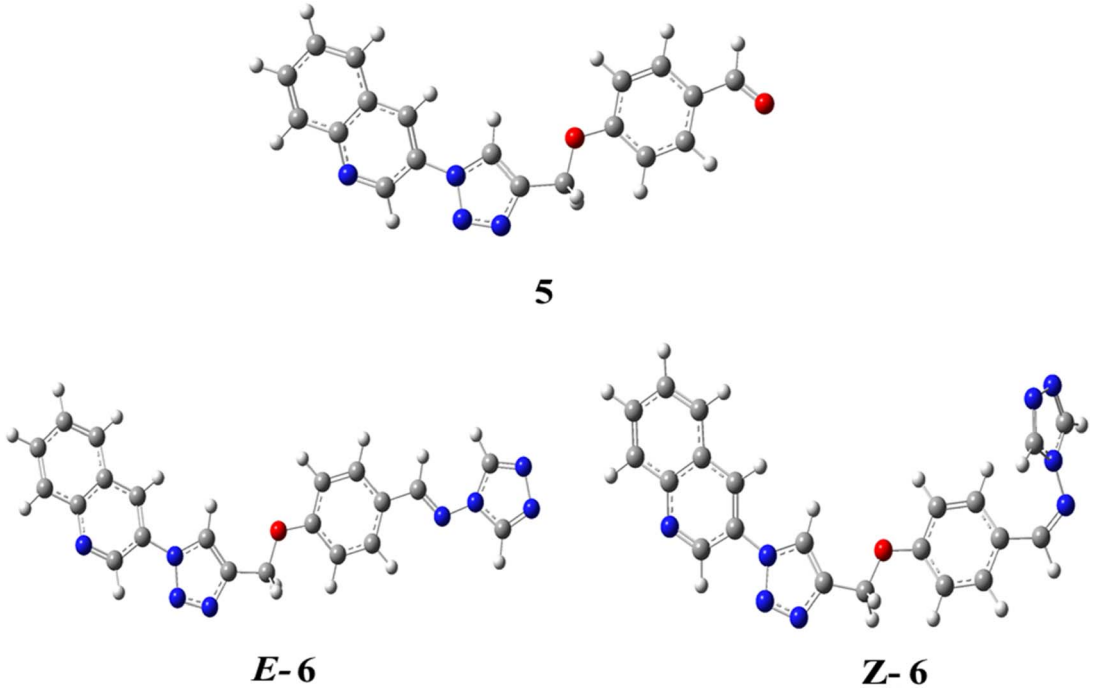

Fig. 6 Optimized geometrical structures of **5** and the two possible geometrical isomers of **6** (grey, carbon; white, hydrogen; red, oxygen; and blue, nitrogen).

Table 2 Calculated thermodynamic parameters for isomers *E*-**6** and *Z*-**6**[a]

Thermodynamic parameter	*E*-6	*Z*-6
E	−1323.022	−1323.011
ZPVE	0.349	0.349
E_{tot}	−1322.673	−1322.662
H	−1322.648	−1322.638
S	179.022	174.753
G	−1322.734	−1322.721

[a] *E*, total electronic energy; ZPVE, zero-point vibrational energy; E_{tot}, total energy (*E* + ZPVE); *H*, enthalpy; *S*, entropy; *G*, Gibbs free energy. All energies are reported in [a.u.], entropy is reported in [cal $(mol \cdot k)^{-1}$].

3.1.1. Nanoencapsulation (CNPs 5* and 6*). With compounds **5** and **6** in hands, both were prepared at the nanometer scale *via* the ionotropic gelation technique. Chitosan nanoparticles (CNPs) loaded with compounds **5** or **6** were synthesized *via* ionic gelation, a method driven by electrostatic attraction (Scheme 2). Chitosan was dissolved in acetic acid, protonating its amine groups to generate a positively charged solution. A solution of the target compound was then incorporated into this cationic chitosan solution to ensure the initial interaction required between the active compound and the chitosan. The mixture was cross-linked by the controlled addition of sodium tripolyphosphate (TPP) under constant stirring. The immediate formation of an opalescent suspension indicated the successful precipitation of loaded nanoparticles **5*** and **6***, resulting from ionic interaction between the NH_3^+ groups at C-2 positions on the glucan ring of chitosan and the anions of TPP.

The particle size and morphology of the compound-loaded chitosan nanoparticles (CNPs **5*** and **6***) were determined by transmission electron microscopy (TEM) (Fig. 3). The analysis confirmed the formation of homogeneous, spherical nanoparticles with a narrow size distribution in the range of 35–43 nm.

The zeta potential (ζ) was measured to evaluate the surface charge and colloidal stability of the nanoparticles. The unloaded chitosan nanoparticles displayed a value of +33.7 mV, which confirms the expected positive surface charge imparted by the protonated amine groups of chitosan in acidic medium.[33] A significant and unexpected finding was the increase in zeta potential following compound encapsulation, with values rising to +35.6 mV and +39.2 mV for CNPs **5*** and **6***, respectively (Fig. 4). This increase suggests that the compounds **5** and **6** contribute additional positive charge to the nanoparticle system, whether through surface association, partial surface exposure, or encapsulation within the chitosan matrix. The enhancement of surface potential is consistent with the molecular electrostatic potential (MEP) maps of the compounds (see later), which reveal regions of positive electrostatic potential. Consequently, both loaded formulations exhibit a stronger positive charge than unloaded chitosan nanoparticles. According to DLVO theory,[34] this elevated charge translates to powerful electrostatic repulsion between particles. With all zeta potential values substantially exceeding +30 mV stability threshold, it can be concluded that CNPs **5*** and **6*** possess excellent colloidal

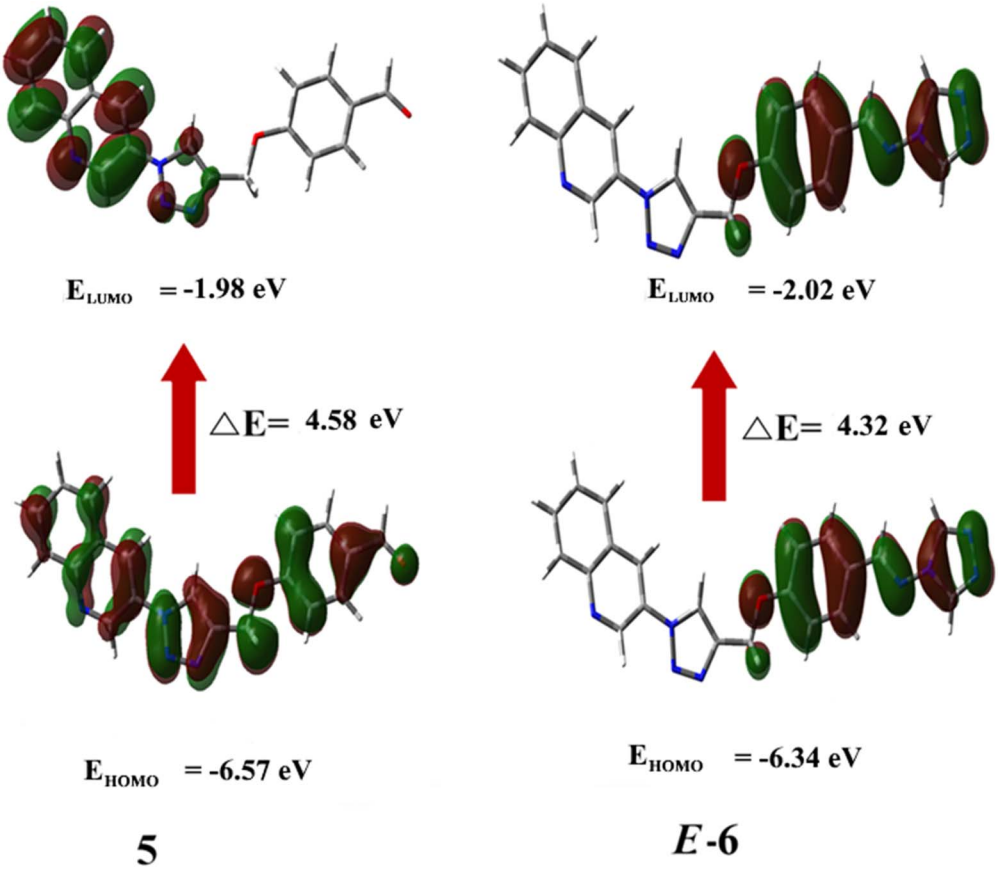

Fig. 7 Frontier molecular orbitals (HOMO and LUMO) of **5** and ***E*-6**.

Table 3 Calculated FMOs energies and associated reactivity descriptors for **5** and ***E*-6**[a]

Parameter	5	*E*-6
E_{HOMO}	−6.57	−6.34
E_{LUMO}	−1.98	−2.02
$\Delta E_{LUMO-HOMO}$	4.58	4.32
I	6.57	6.34
A	1.98	2.02
μ	−4.72	−4.18
χ	4.72	4.18
η	2.29	2.16
ω	3.99	4.04
S	0.44	0.46
ΔN	1.86	1.93

[a] E_{HOMO}, energy of the highest occupied molecular orbital; E_{LUMO}, energy of the lowest unoccupied molecular orbital; $\Delta E_{LUMO-HOMO}$ energy gap ($E_{LUMO} - E_{HOMO}$); I, ionization potential ($-E_{HOMO}$); A, electron affinity ($-E_{LUMO}$); μ, electronic chemical potential (($E_{HOMO} + E_{LUMO}$)/2); χ, electronegativity ($-\mu$); η, hardness (($E_{LUMO} - E_{HOMO}$)/2); S, softness ($1/\eta$); ω, electrophilicity index ($\mu^2/2\eta$); ΔN, fractional number of electrons transferred ($-\mu/\eta$). Energies are reported in (eV).

stability, a critical property for their further application and storage.

Furthermore, the highly observed zeta potentials values are advantageous, and we hypothesize that the strong positive surface charge may promote electrostatic attraction to the negatively charged residues present in the active sites of the targeted enzymes (α-glucosidase and α-amylase) and to the negatively charged cell membranes, potentially improving both inhibitory binding and cellular uptake,[35] which could increase the intracellular bioavailability to potentiate glucose uptake enhancement and antioxidant effects.

3.1.1.1. Encapsulation efficiency (EE%) and drug loading (DL%). The encapsulation efficiency (EE%) and drug loading (DL%) of both nanoformulations are summarized in Table 1. **CNPs 5*** and **6*** exhibited remarkably high EE% values of 99.59% and 99.93%, respectively, indicating near-complete drug entrapment with minimal free drug remaining in the supernatant. The corresponding DL% values were 9.1% and 9.3%, which align closely with the theoretical maximum of 9.09% based on the initial drug-to-chitosan mass ratio (1 : 10 w/w).

The high encapsulation efficiency is attributed to strong electrostatic interactions between the positively charged amino groups of chitosan and the drug molecules, facilitated by the ionic gelation method, which promotes efficient polyelectrolyte complex formation.[36] This is further supported by the increased zeta potential observed upon drug loading. The close agreement between experimental and theoretical DL% values shows that the ionic gelation process enabled near-quantitative

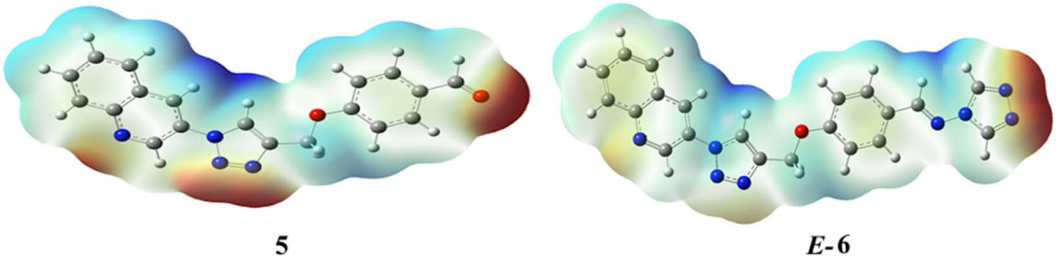

Fig. 8 MEP surface map of **5** and ***E*-6**, color gradient: red (δ^-) < yellow (neutral) < blue (δ^+).

Table 4 *In vitro* biological evaluation for compounds **5**, **6**, **5***, and **6*** on α-amylase, α-glucosidase inhibition, and glucose uptake[a]

	(IC_{50} μM ± SD)		(EC_{50} μM ± SD)
Compound	α-Amylase	α-Glucosidase	Glucose uptake
5	**2.79 ± 0.21**	308.76 ± 0.34	711.36 ± 0.14
6	**0.53 ± 0.03**^{b}	271.94 ± 0.08^{b}	**77.64 ± 0.23**^{b}
5*	**2.47 ± 0.57**^{b,c}	**58.21 ± 0.19**^{b,c}	148.39 ± 0.02^{b,c}
6*	**0.17 ± 0.06**^{b,c,d}	**93.51 ± 0.06**^{b,c,d}	**69.77 ± 0.07**^{b,c,d}
Acarbose	25.08 ± 0.76^{b,c,d,e}	68.91 ± 0.43^{b,c,d,e}	—
Berberine	—	—	115.37 ± 0.09^{b,c,d,e}

[a] Values are expressed as mean ± SD ($n = 3$). Different letters in the same column are significantly different at $p < 0.05$. b: *vs.* **5**; c: *vs.* **6**; d: *vs.* **5***; e: *vs.* **6***.

Table 5 *In vitro* antioxidant evaluation for compounds **5**, **6**, **5***, and **6*** on NO and DPPH[a]

	(IC_{50} μM ± SD)	
Compound	NO	DPPH
5	778.27 ± 0.07	386.86 ± 0.23
6	**270.93 ± 0.27**^{b}	**138.75 ± 0.19**^{b}
5*	573.03 ± 0.10^{b,c}	249.55 ± 0.49^{b,c}
6*	**222.75 ± 0.20**^{b,c,d}	**53.00 ± 0.07**^{b,c,d}
Ascorbic acid	396.66 ± 0.05^{b,c,d,e}	40.10 ± 0.32^{b,c,d,e}

[a] Values are expressed as mean ± SD ($n = 3$). Different letters in the same column are significantly different at $p < 0.05$. b: *vs.* **5**; c: *vs.* **6**; d: *vs.* **5***; e: *vs.* **6***.

incorporation of both drug and chitosan into the nanoparticle matrix, with negligible loss during purification.[37] Collectively, these results demonstrate the robustness of the developed nanocarrier system and its suitability for efficient entrapment of both drug hybrids.

3.1.2. Density functional theory (DFT) studies

3.1.2.1. Energetics and stabilities. DFT calculations were employed to investigate the molecular structure and the electronic properties of compound **5** and the two possible geometrical isomers of compound **6** (***E*-6** and ***Z*-6**) as shown in Fig. 5.[38]

The initial structures were drawn using GaussView 6.016 and subsequently optimized using the B3LYP/6-31G(d,p) method in Gaussian 09 Revision A.02.[39] This computational approach enabled full geometrical optimization to converge, allowing the identification of the most stable and lowest-energy isomer. The resulting optimized structures for compound **5** and the two geometrical isomers of compound **6** are shown in Fig. 6.

The relative thermodynamic stability of the two geometric isomers of compound **6** (***E*-6** and ***Z*-6**) was thoroughly evaluated using DFT calculations, with the complete set of resulting parameters detailed in Table 2.

The computational data provides a coherent and definitive picture, demonstrating that the *E*-isomer (***E*-6**) is thermodynamically preferred over its *Z*-configured counterpart (***Z*-6**). This conclusion is supported by the lower total electronic energy for isomer ***E*-6**, calculated to be 6.841 kcal mol^{-1} lower than that of ***Z*-6**. The enhanced stability of the *E*-configuration is further supported by its more negative values for two other key thermodynamic functions, enthalpy (*H*) and Gibbs free energy (*G*). The more negative enthalpy suggests stronger and more favorable bonding interactions within the structure of ***E*-6**. Most critically, the more negative Gibbs free energy indicates that ***E*-6** is the more stable isomer at equilibrium, as this parameter incorporates both the enthalpy and the entropy (*S*) of the system. The slightly lower entropy value calculated for the *Z*-isomer (***Z*-6**) itself is indicative of a more rigid and conformationally constrained molecular structure. The synergy between these results, lower energy, more negative enthalpy and Gibbs free energy, presents compelling evidence that the *E*-isomer is the predominant stable form. The notable energy difference is explained by the significant steric hindrance inherent to the *Z*-configuration, where bulky molecular groups are forced into closer proximity, resulting in destabilizing repulsive forces that are absent in the more spatially accommodating *E*-isomer.

3.1.2.2. Frontier Molecular Orbitals (FMOs) analysis. FMOs analysis was performed on both compound **5** and the optimized structure ***E*-6**, to elucidate their reactivity. The FMOs are critical for predicting electron transfer and excitation processes, governed by the energy gap ($\Delta E = E_{LUMO} - E_{HOMO}$) between them.[40] A large HOMO–LUMO gap is associated with high kinetic stability and low chemical reactivity, as it requires more energy for electron excitation. On the contrary, a small gap facilitates the electron excitation and indicates higher chemical reactivity. As shown in Fig. 7, the calculated HOMO and LUMO surfaces for **5** and ***E*-6** provide a visual representation of these electron donor and acceptor sites.

Moreover, several key quantum chemical descriptors were derived from the FMOs energies to quantitatively evaluate the

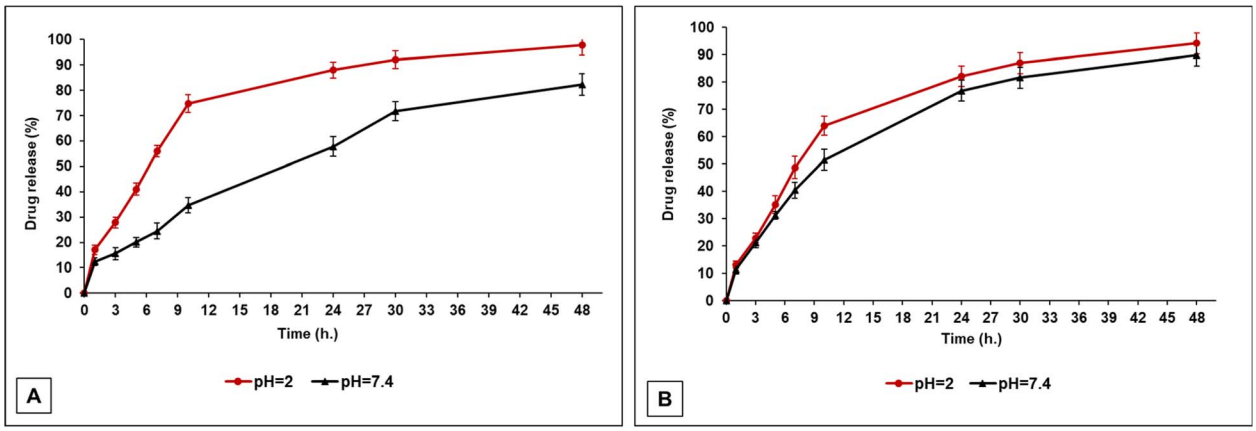

Fig. 9 Drug release profiles for CNPs 5* (A) and 6* (B), at pH = 2 and pH = 7.4 over 48 hours. Results are represented as mean ± SD, $n = 3$.

reactivity of **5** and ***E*-6** (Table 3). The calculated HOMO–LUMO energy gap is higher in **5** (4.58 eV) than in ***E*-6** (4.32 eV).

This reduction in the energy gap indicates that ***E*-6** possesses a higher chemical reactivity and lower kinetic stability than its precursor, **5**, a direct consequence of the extended and more efficient π-conjugation introduced by the imine and the 1,2,4-triazole ring. This trend toward higher reactivity is further quantified by the chemical hardness (η), which is predicted to be higher for **5** (2.29 eV) than for ***E*-6** (2.16 eV), and the global electrophilicity index (ω), which increases slightly from 3.99 eV for **5** to 4.04 eV for ***E*-6**, together confirming that ***E*-6** is a softer and moderately stronger electrophile. This confirms that ***E*-6** is a softer electrophile, meaning it has a greater propensity to form covalent bonds with soft nucleophiles (*e.g.*, thiol groups in biological systems). Furthermore, both compounds exhibit a strong tendency to act as electron acceptors, as evidenced by their positive electron affinity values (A = 1.98 eV for **5** and 2.02 eV for ***E*-6**). This electrophilic character is underscored by the high values for the fraction of electrons transferred (ΔN), which is lower in **5** (1.86 eV) than in ***E*-6** (1.93 eV). This confirms that ***E*-6** is the stronger electrophile of the two. Despite this high reactivity, both molecules display significant stability against oxidation, as reflected by their high ionization potentials (I = 6.57 eV for **5** and 6.34 eV for ***E*-6**), a property conferred by their extensive conjugated π-systems.

The FMOs profiles provide insight into the general reactivity trends of the synthesized compounds. The smaller HOMO–LUMO energy gap and lower hardness of ***E*-6** suggest higher polarizability and a greater propensity for non-covalent interactions compared to **5**, while the electrophilic character of both compounds suggests potential capability to interact with electron-rich biological environments. These electronic characteristics serve as preliminary computational indicators to help rationalize the biological activity trends discussed in the subsequent sections.

3.1.2.3. Molecular electrostatic potential (MEP) surface mapping. MEP surface maps of compound **5** and the most stable isomer, ***E*-6**, were calculated to visualize their electron density distribution and predict their reactivity behavior.[41] As illustrated in Fig. 8, the MEP map uses a color gradient where red regions correspond to the highest electron density (negative potential), and blue regions indicate the lowest electron density (positive potential).[42] The analysis reveals a pronounced negative charge (red) localized on the oxygen atom of the aldehyde group, the nitrogen atoms of the 1,2,3-triazole ring, and the nitrogen atom of the quinoline ring for compound **5**. For ***E*-6**, a clearly observed negatively charged region was localized on the nitrogen atoms of the 1,2,4-triazole ring, which is consistent with the high electronegativity of nitrogen. In contrast, positive potential (blue) is associated with the aromatic and aliphatic C–H protons. This clear separation of strong positive and negative charges across the molecular structure confirms the high polarity of **5** and ***E*-6**, which is quantitatively supported by their large, calculated dipole moments of 6.0236 and 8.3571 Debye for **5** and ***E*-6**, respectively, with full polarizability data provided in Table S1.

This inherent molecular polarity has direct and significant implications for the observed properties of their nanoformulations **5*** and **6***. The strong, positively charged regions (blue) on the molecule's surface are particularly attracted to the negatively charged phosphate groups of the sodium tripolyphosphate (TPP) cross-linker during the ionic gelation process. This facilitates a robust incorporation of **5** and ***E*-6** into the chitosan matrix. Furthermore, it is proposed that the molecule's high polarity and significant positive charge density allow it to not only be encapsulated but also to orient itself on the surface of the chitosan nanoparticles. As mentioned earlier, the MEP maps of compounds **5** and **6** display regions of positive electrostatic potential, which may contribute to the higher zeta potential values observed for CNPs **5*** (+35.6 mV) and **6*** (+39.2 mV) relative to unloaded chitosan nanoparticles (+33.7 mV). While the exact localization of the compounds (surface-associated *vs.* fully encapsulated) cannot be confirmed from the present data alone, the MEP analysis provides a plausible molecular level rationale for the enhanced surface charge and colloidal stability of the loaded nanoformulations. Further surface-sensitive studies would be required to definitively establish the spatial distribution of the compounds within the nanoformulations.

Table 6 Docking scores of the co-crystallized ligand of each protein target with compounds **5** and **6** and amino acids contributing to interactions

Protein target	Ligand	Docking scores S (kcal mol^{-1})	K_i (μM)	Type of binding interactions
Pancreatic α-amylase (PDB ID: 4GQR)	**Myricetin**	−5.60	77.53	2 CHB (Asp197) 1 CHB (Asp300) 1 CHB (Trp59) 1 CHB (Gln3) 1 UAA (Gln63)
	Acarbose	−5.70	66.3	1 CHB (Tyr62) 1 CHB (Asp197) 1 CHB (Glu233) 1 CHB (Asp300) 1 CHB (His305) 1 C–H bond (Tyr151)
	5	−7.20	5.12	1 CHB (Arg296) 1 CHB (Gly121) 1 CHB (Ser203) 1 π–π stacking (Tyr341) 1 π–π stacking (Phe338) 1 π–alkyl (Trp286) 1UDD (Phe295)
	6	−8.76	0.38	1 CHB (His201) 1 CHB (Arg195) 1 CHB (Asp197) 3 CHB (Glu233) 1 π–π stacking (Trp59) 1 π–alkyl (Ala198) 1 C–H bond (Tyr62) 1 UDD (Ile235)
α- Glucosidase (PDB ID: 5NN5)	**1-Deoxynojirimycin**	−8.20	0.96	2 CHB (Asp518) 1 CHB (His674) 1 UAA (Asp404)
	Acarbose	−7.40	3.77	1 CHB (Leu195) 1 CHB (Glu192) 1 CHB (Asp338) 1 CHB (Lys184) 1 CHB (Glu174) 1 CHB (Tyr340) 1 CHB (His180)
	5	−7.20	5.28	1 CHB (Leu195) 1 CHB (Arg189) 1 CHB (Val193) 1 π–anion (Asp338) 1 π–π T-shaped (Tyr340)
	6	−6.20	27.30	1 CHB (Arg190) 1 CHB (Glu192) 1 C–H bond (Val193) 1 C–H bond (Tyr340) 1 π–alkyl (His180) 1 π–alkyl (Leu195) 1 π – alkyl (Leu313) 1 π–donor HB (Tyr340)
GLUT-4 (PDB ID: 7WSM)	**Cytochalasin B**	−10.71	0.01	1 CHB (Gly400) 1 CHB (Gln298) 1 CHB (Ser153) 1 CHB (Trp404) 1 π–σ (Trp428) 1 π–alkyl (Ile180)
	5	−6.67	12.97	1 CHB (Ser96) 1 CHB (Trp428) 1 π–σ (Ala421) 1 π–alkyl (Ile199)
	6	−6.90	8.90	1 CHB (Glu270) 1 CHB (Gly414)

Table 6 (*Contd.*)

Protein target	Ligand	Docking scores S (kcal mol^{-1})	K_i (μM)	Type of binding interactions
KEAP1-NRF2 (PDB ID: 6TYM)	**CHEMBL4635041**	−10.46	0.02	1 π–cation (Arg228) 1 π–σ (Ile99) 1 amide–π stacked (Met420) 1 CHB (Ser508) 1 salt bridge (Arg415) 1 salt bridge (Arg 483) 1 salt bridge (Phe478) 1 π–π stacking (Tyr525) 1 π–alkyl (Ala556) 1 π DHB (Ser602) 1 UDD (Ser555) 1 UDD (Gln530)
	5	−7.80	1.90	1 CHB (Ser555) 1 CHB (Gln530) 1 CHB (Ala510) 1 C–H bond (Gly509) 1 amide–π stacked (Ser508) 1 π–alkyl (Ala556) 1 π–alkyl (Ala366) 1 π–alkyl (Arg415)
	6	−8.78	0.37	1 CHB (Gly367) 1 CHB (Val463) 1 CHB (Ile416) 1 CHB (Ser508) 1 C–H bond (Ala510) 1 amide–π stacked (Gly462) 1 π–alkyl (Ala336) 1 π–alkyl (Ala556) 1 π–alkyl (Arg415) 1 amide–π stacked (Gly462) 1 UDD (Val418)

3.2. Biological evaluation

3.2.1. Antidiabetic activity. The *in vitro* inhibition of α-glucosidase and α-amylase, key enzymes involved in dietary carbohydrate hydrolysis, represents a therapeutic strategy for modulating postprandial hyperglycemia in T2DM.[43,44] The synthesized compounds **5**, **6**, **5***, and **6*** were evaluated for their inhibitory potential against these enzymes, using acarbose as a reference inhibitor. Additionally, their ability to stimulate cellular glucose uptake was assessed relative to berberine, a well-known enhancer of glucose uptake.

3.2.1.1. In vitro α-amylase inhibitory activity. The α-amylase *in vitro* inhibitory activity of the tested compounds was evaluated by determining their half maximum inhibitory concentration (IC_{50}) values relative to the standard inhibitor acarbose (IC_{50} = 25.08 μM). The results indicated that compounds **5**, **6**, **5***, and **6*** showed substantial inhibitory potential, with **6*** exhibiting the most potent inhibition (IC_{50} = 0.17 μM), followed by **6** (IC_{50} = 0.53 μM), **5*** (IC_{50} = 2.47 μM), and **5** (IC_{50} = 2.79 μM). All four compounds outperformed acarbose. As shown in Table 4, the inhibitory potency was enhanced through structural evolution from compound **5** to compound **6** and further improved in the nanoformulations **5*** and **6***. The notable potency of **6*** may be attributed to the integration of 1,2,4-triazole and 1,2,3-triazole moieties with a quinoline backbone bearing nitrogen atoms that increase the electron density of the aromatic ring, influence the electrostatic interactions with the substrate, and enable hydrogen bonding with various amino acids, combined with its corresponding chitosan-encapsulated formulation. These results are consistent with the molecular docking study (see later).

3.2.1.2. In vitro α-glucosidase inhibitory activity. The α-glucosidase inhibitory activity was evaluated by comparing IC_{50} values to acarbose (IC_{50} = 68.91 μM). Compound **5*** (IC_{50} = 58.21 μM) exhibited potency comparable to acarbose (Table 4). In contrast, its parent compound, **5**, showed markedly weaker activity (IC_{50} = 308.76 μM). The enhanced activity of **5*** may be attributed to its nanoformulation, which likely improves solubility and target site interaction. The retained aldehyde functional group could also act as a key pharmacophore serving as a hydrogen bond acceptor and potentially participating in reversible covalent interactions with different nucleophilic residues in the target enzyme's active site, a hypothesis supported by subsequent molecular docking studies. Compound **6*** demonstrated moderate inhibition (IC_{50} = 93.51 μM), which was still significantly stronger than its parent compound **6** (IC_{50} = 271.94 μM). This result further highlights the beneficial role of nanoformulation in boosting activity.

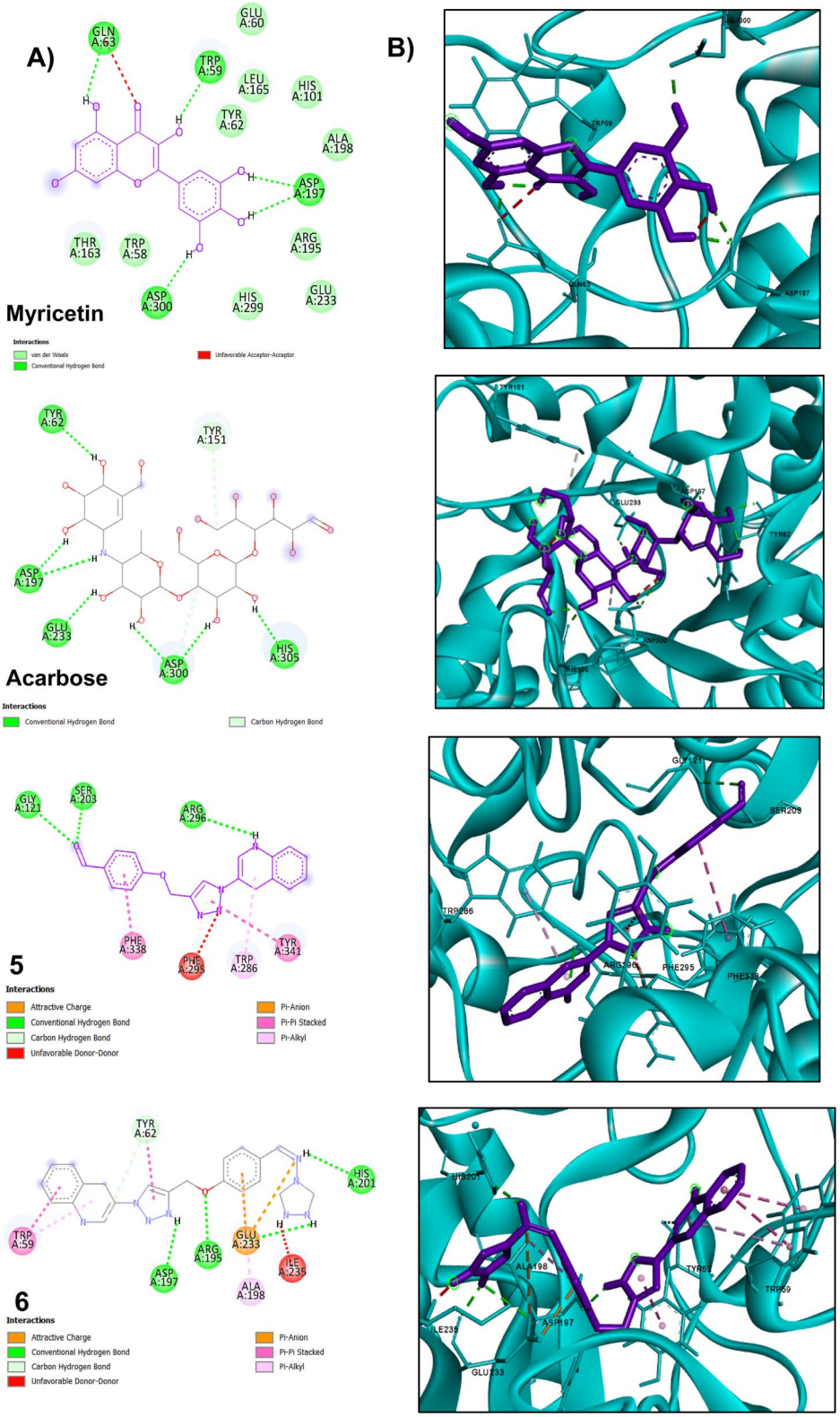

Fig. 10 (A) 2D and (B) 3D representations of docking interactions of myricetin, acarbose, **5** and **6** within the binding pocket of α-amylase (PDB ID: 4GQR).

3.2.1.3. In vitro glucose uptake assay. The hypoglycemic potential of the compounds was assessed *via* a yeast cell glucose uptake assay using *Saccharomyces cerevisiae*, in which residual glucose in the medium was measured after incubating yeast cells with various compound concentrations. *S. cerevisiae* represents a well-established *in vitro* model for preliminary

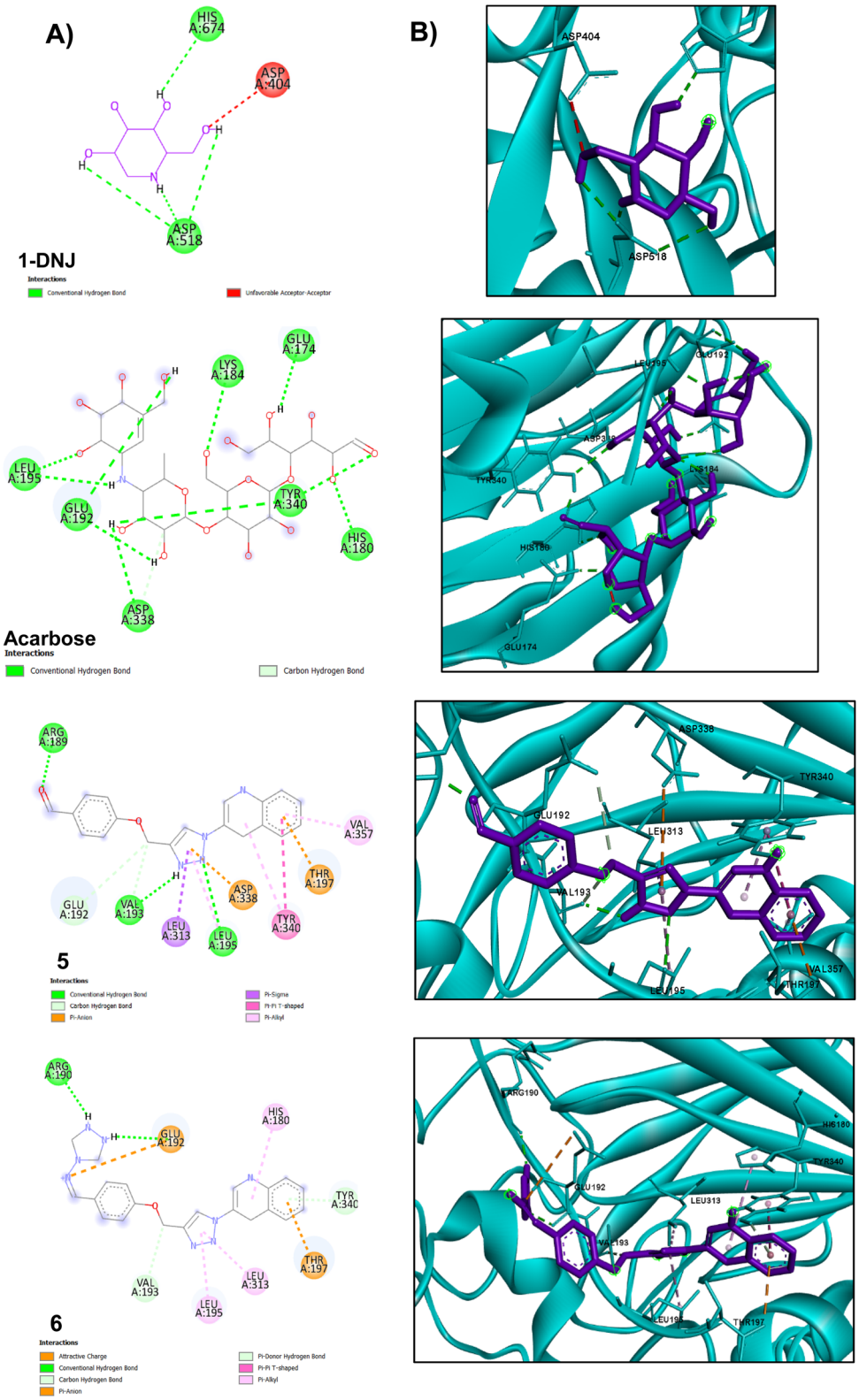

Fig. 11 (A) 2D and (B) 3D representations of docking interactions of 1-deoxynojirimycin, acarbose, **5** and **6** within the binding pocket of α-glucosidase (PDB ID: 5NN5).

antidiabetic screening.[45–48] In this model, glucose uptake occurs primarily through facilitated diffusion *via* membrane carriers that are conceptually similar to human GLUT transporters.[46] Additionally, intracellular glucose is rapidly metabolized, maintaining a low internal glucose concentration that favors continued uptake.[49] A lower residual extracellular glucose

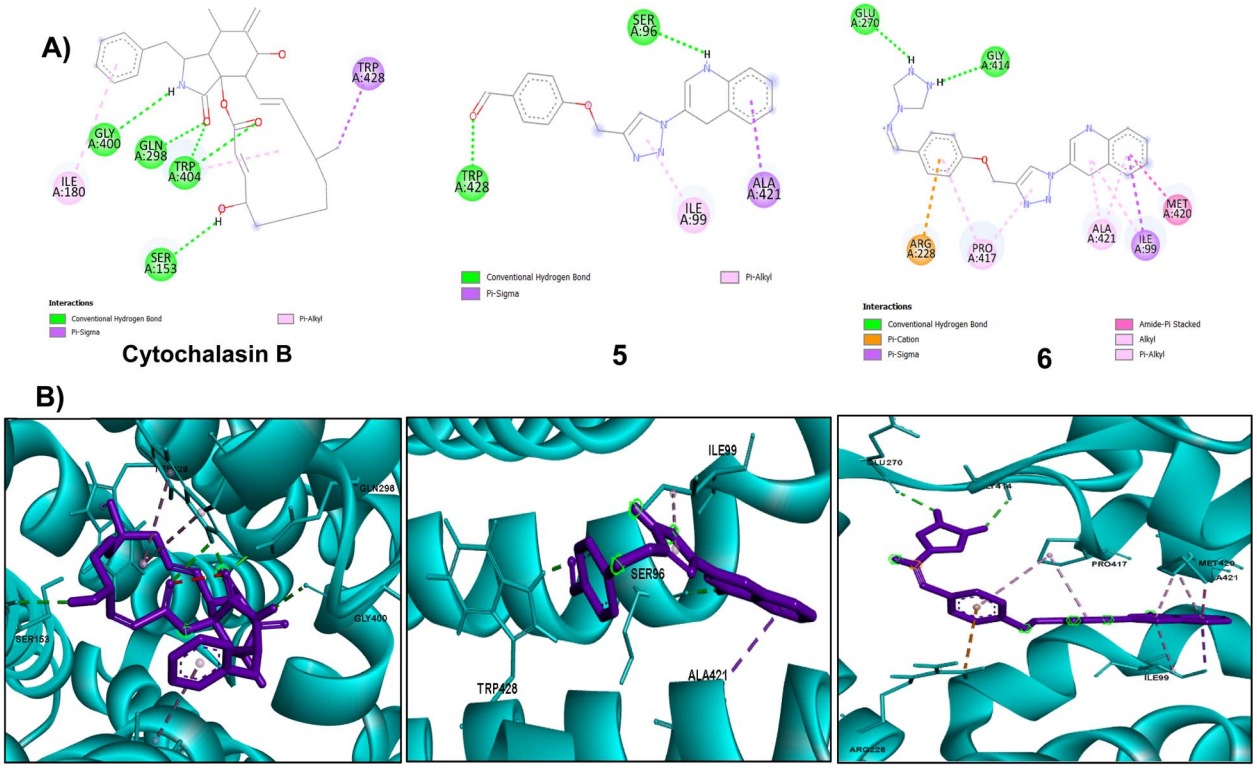

Fig. 12 (A) 2D and (B) 3D representations of docking interactions of cytochalasin B, **5** and **6** within the binding pocket of GLUT-4 (PDB ID: 7WSM).

concentration following incubation is therefore interpreted as an indicator of antidiabetic potential and relative compound potency compared to reference medications. It should be noted, however, that this model does not recapitulate the hormonal, immune, or insulin-signaling context of mammalian physiology,[46,48,49] and these findings should be considered

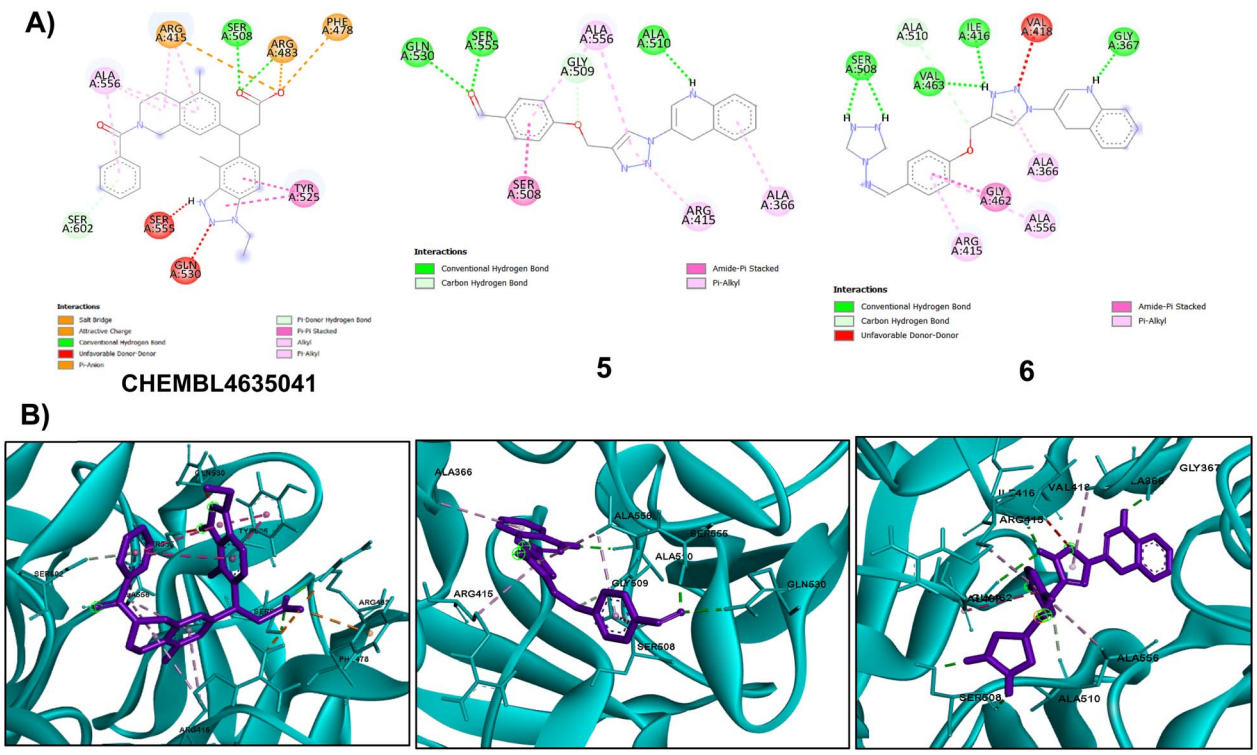

Fig. 13 (A) 2D and (B) 3D representations of docking interactions of CHEMBL4635041, **5** and **6** within the binding pocket of KEAP1 (PDB ID: 6TYM).

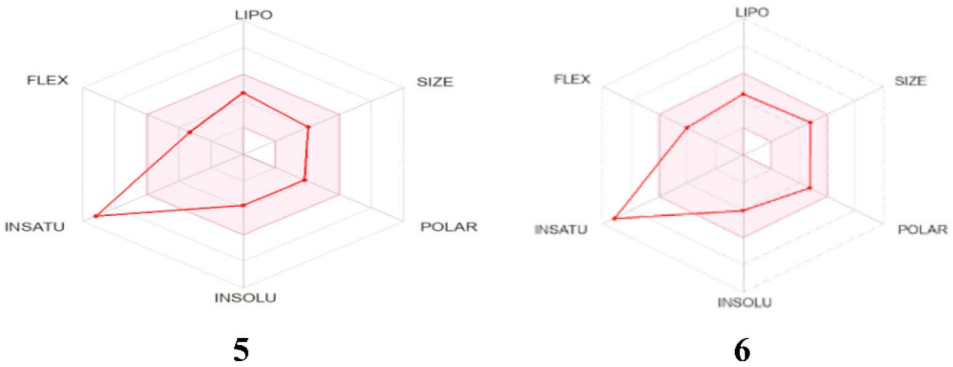

Fig. 14 Bioavailability radar (polar plot) for compounds **5** and **6**.

Table 7 Calculated physicochemical properties of **5** and **6**[a]

	Compounds	
Property	**5**	**6**
MWt (g mol^{-1})	330.35	396.41
Consensus log P_o/w	2.63	2.43
Log S	−3.81	−4.02
XLOGP3	2.58	2.35
WLOGP	3.06	2.72
TPSA (Å^2)	69.9	95.9
*n*HBA	5	7
*n*HBD	0	0
*n*NRB	5	6
Heavy atoms	25	30
Aromatic heavy atoms	21	26
FCsp^3	0.05	0.05

[a] MWt, molecular weight; consensus log P_o/w, logarithm of the octanol/water partition coefficient, a measure of lipophilicity; log S, aqueous solubility; XLOGP3, extended atom-type based (version 3), a measure of lipophilicity; WLOGP, Wildman and Crippen LogP, a measure of lipophilicity; TPSA, topological polar surface area; nHBA, number of H-bond acceptors; nHBD, number of H-bond donors; nNRB, number of rotatable bonds; FCsp^3, fraction Csp^3, carbon atoms with sp^3 hybridization.

preliminary evidence warranting further validation in mammalian cell-based and *in vivo* models.

Activity was expressed as the half-maximal effective concentration (EC_{50}) relative to the reference enhancer berberine (EC_{50} = 115.37 μM), as summarized in Table 4. Compounds **6** and **6*** displayed significant activity with EC_{50} values of 77.64 and 69.77 μM for **6** and **6***, respectively. These values correspond to potencies that were ∼1.48- and ∼1.65-fold higher, respectively, than that of berberine. Compound **5*** (EC_{50} = 148.39 μM) exhibited lower but notable glucose uptake enhancement, whereas compound **5** demonstrated weak activity (EC_{50} = 711.36 μM). The improved performance of the nanoformulated compounds implies that nanoscale delivery may facilitate cellular interaction and glucose transport modulation, supporting the contribution of formulation and molecular architecture to antihyperglycemic activity.

3.2.2. Antioxidant activity. Reactive oxygen species (ROS), generated through endogenous metabolic processes or exogenous stress, contribute to oxidative damage when their production exceeds the cellular antioxidant capacity. The pathological accumulation of ROS is implicated in the pathogenesis of several chronic diseases, including diabetes mellitus and cardiovascular disorders.[50–52] Therefore, the antioxidant potential of the synthesized compounds was evaluated *in vitro*

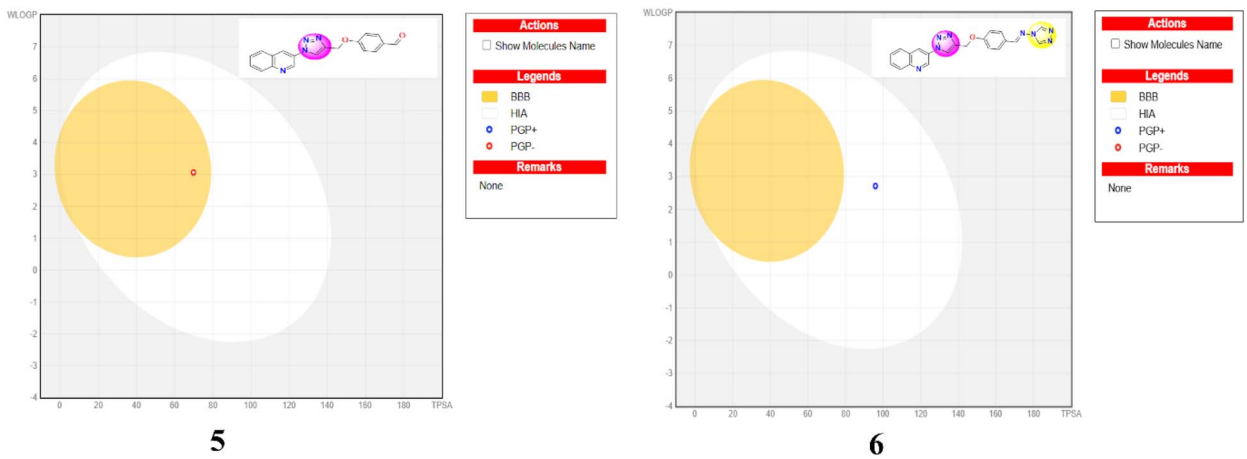

Fig. 15 The boiled-egg predictive model for compounds **5** and **6**.

using nitric oxide (NO) and 2,2-diphenyl-1-picrylhydrazyl (DPPH) radical scavenging assays, with ascorbic acid employed as a reference standard antioxidant.

3.2.2.1. NO scavenging activity. NO scavenging capacity was evaluated by determining the half-maximal inhibitory concentration (IC_{50}) relative to ascorbic acid (IC_{50} = 396.66 μM). Compared to **5** and **5***, compound **6** and its nanoformulated counterpart **6*** demonstrated significant NO scavenging activity, exhibiting ~1.46- and ~1.78-fold higher potency than ascorbic acid, respectively (Table 5).

This significant activity is attributed to the electron-rich, polyheterocyclic system, where multiple nitrogen atoms facilitate direct radical sequestration *via* electron transfer, and the formation of stabilized radical adducts. This aligns with the pronounced electron-rich (negative, red) regions localized on nitrogen atoms, as visualized in the MEP maps of the parent compounds (Fig. 8). The extended π-conjugation within the framework promotes delocalization and stabilization of the unpaired electron following interaction with the NO radical. Additionally, the nitrogen-dense structure may act as a polydentate ligand, enabling secondary antioxidant mechanisms through metal chelation and modulation of redox pathways.

The marked efficacy of the chitosan-encapsulated derivative **6*** suggests that nanoformulation enhances bioavailability or interfacial access to radical species, thereby potentiating the intrinsic pharmacodynamic activity. In contrast, compounds **5** and **5*** exhibited weaker scavenging activity compared to the ascorbic acid standard.

3.2.2.2. DPPH radical scavenging activity. The free radical scavenging potential was further assessed using the stable DPPH radical relative to ascorbic acid (IC_{50} = 40.10 μM). While both parent compounds **5** and **6** showed weaker DPPH scavenging than the standard, compound **6** was ~2.8-fold more potent than **5**, a trend consistent with the NO scavenging results (Table 5). Consistent with the other assays, nanoencapsulation significantly enhanced activity. Compound **6*** displayed considerable scavenging (IC_{50} = 53.00 μM), representing the best activity among all tested compounds and a notable improvement over its parent, **6** (IC_{50} = 138.75 μM). The observed trend aligns with the structure–activity relationship (SAR) proposed for NO scavenging, wherein the introduction of an extra triazole moiety in **6** provides a more effective electron-dense pharmacophore for neutralizing free radicals *via* hydrogen atom transfer or single-electron transfer mechanisms.

3.2.3. *In vitro* drug release profiles of CNPs 5* and 6*. The *in vitro* drug release profiles of **CNPs 5*** and **6*** were evaluated at pH 2.0 (simulated gastric fluid) and pH 7.4 (simulated intestinal fluid) over 48 hours, as shown in Fig. 9. Both nanoformulations displayed a clear pH-dependent release behavior, with markedly faster and more extensive drug release under acidic conditions. At pH 2.0, **CNPs 5*** exhibited a rapid initial release, reaching 55.9% within 7 hours and 87.9% by 24 hours, with near-complete release (97.8%) achieved at 48 hours (Fig. 9A). **CNPs 6*** followed a similar trend at pH 2.0, reaching 48.7% at 7 hours and 94.3% at 48 hours (Fig. 9B). Under physiological pH (pH = 7.4), drug release was considerably more sustained, **CNPs 5*** and **6*** released 24.5% and 40.5% of their payload by 7 hours, respectively, rising gradually to 82.4% and 89.9% by 48 hours.

The observed pH-dependent release is consistent with the known swelling behavior of chitosan under acidic conditions, where protonation of the amino groups leads to polymer chain relaxation and enhanced drug diffusion.[53] Notably, **CNPs 6*** exhibited a slightly more gradual release profile at pH 2.0 and a higher cumulative release at pH 7.4 compared to **CNPs 5***, which may reflect differences in drug–polymer interactions or the marginally higher drug loading of this formulation. The biphasic release pattern, an initial burst phase followed by sustained release, observed for both formulations is characteristic of chitosan-based nanoparticulate systems and is advantageous for oral delivery, where an initial therapeutic dose may be followed by prolonged drug availability. These results indicate that both nanoformulations exhibit pH-responsive release behavior, which may be advantageous for oral drug delivery applications.

4. *In silico* studies

4.1. Molecular docking studies

4.1.1. Antidiabetic and antioxidant potential. To predict the binding affinity and inhibitory potential of the synthesized compounds, molecular docking simulations were performed against four key molecular targets implicated in diabetes and oxidative stress. Prior to docking, the protocol was validated by re-docking of the co-crystallized ligands into their respective binding sites; the resulting root-mean-square deviation (RMSD) values ranged from 0.31 Å to 1.73 Å, all well below the accepted threshold of 2.0 Å, confirming the reliability of the protocol in reproducing the bioactive ligand conformations (Table S2 and Fig. S9). The binding energies and predicted inhibition constants (K_i) for both compounds **5** and **6** were compared with their respective co-crystallized reference ligands (Table 6).

4.1.1.1. α-Amylase docking interactions. For pancreatic α-amylase (PDB ID: 4GQR), both compounds demonstrated superior binding affinity compared to the reference ligand Myricetin (S = −5.60 kcal mol; K_i = 77.53 μM), which forms hydrogen bonds with Asp197 and Asp300; however, its affinity is compromised by a destabilizing repulsion (unfavorable acceptor–acceptor interaction) between its carbonyl oxygen and Gln63. For a direct comparison with the standard reference inhibitor, acarbose was also docked into the same binding site, yielding a docking score of −5.70 kcal mol^{-1}, with conventional hydrogen bond interactions with key residues Tyr62, Asp197, Glu233, Asp300, and His305, alongside a C–H bond with Tyr151. Both synthesized compounds outperformed acarbose, consistent with the *in vitro* inhibition data. Notably, compound **6** showed the most potent interaction, with a binding energy of −8.76 kcal mol^{-1} and predicted inhibition constant of 0.38 μM. This strong inhibition may be attributed to conventional hydrogen bonds with key catalytic residues Glu233, Asp197, His201 and Arg195, suggesting strong inhibitory potential against starch hydrolysis. As shown in Fig. 10, compound **5** also outperformed both acarbose and the reference ligand, exhibiting a binding energy of −7.20 kcal mol^{-1} (K_i = 5.12 μM). This

favorable binding is likely due to maintaining 3 conventional hydrogen bonds with Gly121, Ser203, Arg296, alongside an unfavorable interaction with Phe295.

4.1.1.2. α-Glucosidase docking interactions. In the case of α-glucosidase, the reference inhibitor 1-deoxynojirimycin (1-DNJ) retained the highest binding affinity ($S = -8.20$ kcal mol^{-1}). As a carbohydrate mimic, its high potency is attributed to the formation of a dense, multipoint hydrogen-bonding network that specifically anchors the ligand to the catalytic residues Asp518 and His674. For additional clinical context, acarbose was docked into this target, producing a score of −7.40 kcal mol^{-1} with conventional hydrogen bond interactions with Leu195, Glu192, Asp338, Lys184, Glu174, Tyr340, and His180. In contrast, the synthesized derivatives exhibited distinct binding modes driven by their non-sugar scaffolds. Compound **5** showed a docking score comparable to that of acarbose ($S = -7.20$ kcal mol^{-1}), stabilizing its conformation through a triad of conventional hydrogen bonds with Arg189, Val193, and Leu195. Conversely, compound **6** demonstrated reduced binding affinity ($S = -6.20$ kcal mol^{-1}), which may be attributed to a less extensive polar interaction network. Its stabilization relied primarily on two hydrogen-bond interactions with Arg190 and Glu192. These findings suggest that, although compound **5** achieves a favorable and viable fit within the α-glucosidase active site, the scaffold of compound **6** is less complementary to the enzyme pocket when compared to the native substrate mimic as illustrated in Fig. 11. It is worth mentioning that the docking results contradicting the *in vitro* inhibition data of α-glucosidase where **6** is more potent than **5**. This discrepancy likely arises from a key limitation of rigid-receptor docking. The extended, flexible scaffold of **6**, may require significant conformational adaptation of the enzyme's active site (induced-fit) to achieve its optimal bioactive pose. The static model fails to capture this, penalizing **6** larger size while favoring the more compact **5**. As a result, the computational model successfully identifies **5** as a competent binder but underestimates the true inhibitory potential of the more flexible and biophysically adaptive hybrid **6**.

4.1.1.3. GLUT-4 docking interactions. In the case of GLUT-4 transport inhibition (PDB ID: 7WSM), a distinct hierarchy in binding efficacy was observed. The reference standard, cytochalasin B, exhibited superior binding affinity ($S = -10.71$ kcal mol^{-1}). This high affinity is attributed to its ability to deeply occlude the central glucose transport channel through critical hydrogen-bond interactions with Gln298 and Trp404. In contrast, the synthesized derivatives adopted vestibular binding poses with moderate affinities and lacked the deep channel-locking mechanism observed for the cytochalasin B. Compound **6** ($S = -6.90$ kcal mol^{-1}) established a unique electrostatic interaction profile, primarily anchored by a high-energy π-cation interaction with Arg228, in addition to conventional hydrogen bonds with Glu270 and Gly414. This electrostatic network provided a slight energetic advantage over compound **5** ($S = -6.67$ kcal mol^{-1}), which relied mainly on peripheral hydrogen-bond interactions with Trp428 and Ser96. Overall, the observed structural divergence suggests that while **6** may function as a specific GLUT-4 modulator through anchoring at Arg228, it does not achieve the complete steric blockade of the glucose transport channel that characterizes the high-affinity reference inhibitor, as shown in Fig. 12.

4.1.1.4. KEAP1 docking interactions. For the antioxidant regulator KEAP1–NRF2 complex (PDB ID: 6TYM), molecular docking assessment revealed a clear structure–activity relationship (SAR) governing the predicted Nrf2 displacement potential. The co-crystallized reference ligand exhibited the highest binding affinity ($S = -10.46$ kcal mol^{-1}), which is attributed to a strong electrostatic "clamping" mechanism. In this interaction, carboxylate groups form critical salt bridges with a deep arginine cluster composed of Arg415 and Arg483. Compound **6** emerged as a promising lead compound ($S = -8.78$ kcal mol^{-1}). Its enhanced potency is driven by a robust hydrogen-bonding network anchored to the key hotspot residue Ser508, in combination with a strategically positioned π–alkyl interaction that provides hydrophobic shielding of Arg415. While compound **5** also demonstrated favorable binding ($S = -7.80$ kcal mol^{-1}), it showed a weaker interaction profile. Although both compounds interacted with key surface residues neither fully penetrated penetrate the central binding cavity or engage the arginine triad required for high-affinity KEAP1 inhibition like the reference ligand. This observation highlights the challenge of achieving deep pocket occupancy and suggest that the triazole–quinoline scaffold in **6** provides a more effective partial distribution of the KEAP1–Nrf2 interaction as illustrated in Fig. 13.

4.2. Physicochemical, pharmacokinetics and ADME properties

Analysis of the drug-likeness, physicochemical properties, and pharmacokinetic profiles of compounds **5** and **6** was conducted using the Swiss ADME tool.[54] A radar graph illustrates the chemical structure and the drug-likeness of both compounds, **5** and **6**, by mapping key molecular features, lipophilicity (XLOGP3), size (expressed by molecular weight), polarity (TPSA), solubility (log *S*), saturation (fraction Csp3), and flexibility (number of rotatable bonds), on six axes. The pink hexagonal area represents the optimal range for each property to ensure oral bioavailability, while the coloured polygon represents the actual calculated profile of the compound (Fig. 14). As presented in Table 7, both compounds obey Lipinski's rule of five,[55] with favorable molecular weights of ∼330 and 396 g mol^{-1}, consensus log P_o/w of ∼2.6 and 2.4, and TPSA of ∼70 and 96 Å^2. However, their low sp^3 carbon fraction (0.05) and high aromaticity indicate a planar structure (as shown in the DFT optimized geometries, Fig. 6), which correlate with their predicted poor aqueous solubility (log $S \sim -3.8$ and −4). This represents a notable developability liability, as such low solubility values fall well below the typically acceptable range for orally administered drugs and may require advanced formulation strategies to achieve adequate bioavailability.

A boiled-egg plot was designed to evaluate the relationship between the calculated (WLOGP), also known as Wildman and Crippen lipophilicity, and the topological polar surface area (TPSA) of the studied compounds, providing predictions of

gastrointestinal (GI) absorption and blood–brain barrier (BBB) penetration. The WLOGP parameter estimates the compound's distribution between aqueous and lipid phases, while TPSA quantifies the polar surface area, which is predominantly determined by oxygen and nitrogen atoms and inversely correlates with passive membrane permeability.[56] The plot features three different zones: white, yellow, and gray. The yellow zone (yolk) shows compounds predicted to have high BBB permeability, whereas the white zone indicates high probability of GI absorption, and the grey zone corresponds to compounds with low predicted absorption and negligible brain penetration.

As illustrated in Fig. 15 and Table S3 (see SI), both compounds display a mixed pharmacokinetic profile with distinct strengths and liabilities. Compound **5** is predicted to have high gastrointestinal (GI) absorption, good oral bioavailability, and the ability to cross the BBB, positioning it within the yellow (BBB+) zone of the boiled-egg plot. Its status as a non-substrate for the P-glycoprotein (P-gp) efflux transporter further supports effective brain penetration, suggesting potential as a CNS-active agent. However, this promising profile is significantly offset by a critical metabolic liability as it is predicted to inhibit all five major cytochrome P450 isoforms tested (CYP1A2, 2C19, 2C9, 2D6, 3A4). This pan-CYP inhibition indicates a high potential for clinically significant drug–drug interactions, which represents a priority for future structural optimization. In contrast, compound **6** also exhibit high GI absorption and good bioavailability but is predicted neither to cross the BBB nor to serve as P-gp substrate, consistent with its location in the white (absorption-only) zone of the boiled-egg plot. This profile is more suitable for peripherally acting therapeutics where CNS exclusion is desired. Its CYP inhibition profile is more selective, affecting only the 2C9 and 3A4 isoforms, presenting comparatively a more manageable drug-interaction risk. However, its P-gp substrate status introduces a potential liability for reduced intracellular exposure in P-gp-overexpressing tissues and possible efflux-mediated drug–drug interactions, which should be investigated further. Overall, while both compounds exhibit promising drug-like parameters, their developability is constrained by a combination of poor aqueous solubility (both compounds), pan-CYP inhibition (compound **5**), and P-gp substrate liability (compound **6**). These limitations should guide the design of subsequent analogues.

5. Conclusion

In summary, motivated by a molecular hybridization strategy, new quinoline-triazole hybrids and their chitosan-encapsulated derivatives were successfully synthesized and evaluated as prospective multitarget antidiabetic agents. *In vitro* enzymatic assays revealed that nano-encapsulation markedly improved inhibitory potency: compound **6*** was the most potent α-amylase inhibitor (IC_{50} = 0.17 μM) and compound **5*** the most effective against α-glucosidase (IC_{50} = 58.21 μM), both surpassing the reference drug acarbose. In glucose uptake stimulation, compound **6*** (EC_{50} = 69.77 μM) outperformed berberine (EC_{50} = 115.37 μM), while also demonstrating the strongest antioxidant activity in both NO and DPPH assays. Both nanoformulations exhibited high encapsulation efficiencies (>99%) and drug loading values close to the theoretical maximum, with pH-dependent drug release profiles favoring release under acidic conditions. Molecular docking revealed key binding interactions within the enzyme active sites, highlighting the contributions of the quinoline-triazole scaffold to the observed inhibitory activities. DFT calculations offered preliminary insights into the electronic properties and stability of the hybrids, and ADME profiling indicated favorable drug-likeness with no violations of Lipinski's rule of five. Collectively, these findings highlight the promising preliminary antidiabetic and antioxidant profiles of the synthesized quinoline-triazole hybrids. While the current study offers promising *in vitro* evaluation and computational insights, *in vivo* validation and systematic structure–activity relationship studies are now required to fully assess the therapeutic viability and safety of these hybrids as future drug candidates.

6. Experimental

6.1. Chemistry

6.1.1. Materials and methods. Unless otherwise stated, all chemicals and solvents were of analytical grade and purchased from Sigma-Aldrich. The progress of all chemical reactions was monitored using Merck TLC precoated silica gel 60 F254 aluminum sheets (20 × 20 cm, Merck KGaA, Darmstadt, Germany). The chromatograms were visualized under UV light at 254 nm. Melting points were determined using a Büchi model B-545 apparatus (Büchi Corporation, Flawil, Switzerland) and were uncorrected. FTIR spectra were recorded with a PerkinElmer 1600 series infrared spectrophotometer (Waltham, MA, USA) using potassium bromide (KBr) pellets, and absorption bands ($\bar{\nu}_{max}$) were reported in wavenumbers (cm^{-1}). ^1H and ^{13}C NMR spectra were recorded at 500 and 125 MHz, respectively, using a JNM-ECZ500R/S1 spectrometer (JEOL) in DMSO-d_6, the deuterated solvent served as an internal deuterium lock, with tetramethylsilane (TMS) as an internal standard for protons and solvent signals. Chemical shift (δ) values are reported in ppm, and coupling constants (J) are given in Hz. High-resolution mass spectra (HRMS) were obtained using an LC/Q-TOF 6530 mass spectrometer (Agilent Technologies, Santa Clara, CA, USA) equipped with an electrospray ionization (ESI) source that operated in positive ion mode. Accurate mass measurements were provided as mass-to-charge ratios (m/z). TEM imaging of Chitosan nano particles was performed on a JEOL JEM-1400 Plus. Zeta potential measurements were recorded with Zetasizer Nano ZS90/ZEN3600 (Malvern Instruments, UK).

6.1.2. Synthesis of 4-((1-(quinolin-3-yl)-1*H*-1,2,3-triazol-4-yl)methoxy)benzaldehyde (5).[57,58] 4-(Prop-2-yn-1-yloxy) benzaldehyde (**4**) (0.62 mmol, 1.00 equiv.) and 3-azidoquinoline (**2**) (0.70 mmol, 1.00 equiv.) were dissolved in THF (15 mL). Sodium ascorbate (0.62 mmol, 1.00 equiv.) and copper(II) sulphate (0.04 mmol, 0.06 equiv.) dissolved in distilled water (2 mL) were then added, and the reaction mixture was stirred at room temperature for 6 h and the reaction progress was monitored by TLC. Upon completion, the mixture was poured into cold water, and the precipitated solid was collected by

filtration, washed with water, and recrystallized from ethanol to afford product **5** as colorless crystals (0.59 mmol, 94% yield).

6.1.3. Synthesis of (*E*)-*N*-(4-((1-(quinolin-3-yl)-1*H*-1,2,3-triazol-4-yl)methoxy)benzylidene)-4*H*-1,2,4-triazol-4-amine (6).[29,59] A mixture of 4-((1-(quinolin-3-yl)-1*H*-1,2,3-triazol-4-yl)methoxy) benzaldehyde (**5**) (0.30 mmol, 1.00 equiv.) and 4-amino-4*H*-1,2,4-triazole (0.60 mmol, 2.00 equiv.) was dissolved in absolute ethanol (20 mL), and a few drops of concentrated H_2SO_4 were added. The reaction mixture was refluxed for 6 h, and the progress was monitored by TLC. Upon completion, the mixture was poured into cold water, and the resulting solid was collected by filtration, washed with water, and recrystallized from ethanol to afford product **6** as colorless crystals (0.27 mmol, 90% yield).

6.1.4. Preparation of CNPs 5* and 6*.[60] Chitosan (250 mg) was dissolved in 50 mL of 1% v/v acetic acid solution (pH 4.8), yielding a final chitosan concentration of 0.5% w/v, and stirred at 1000 rpm for 2 hours at room temperature. Compound **5** or **6** (0.08 mmol) was dissolved in DMSO (4 mL) and added to the chitosan solution, and the mixture was stirred at 1000 rpm for an additional 2 hours at room temperature. A sodium tripolyphosphate (TPP) solution (0.1% w/v in deionized water) was then added dropwise to the chitosan mixture (chitosan : TPP mass ratio of 3 : 1) under stirring at 1000 rpm for 12 hours or until equilibrium was reached. The resulting opalescent suspension was allowed to settle, and the chitosan nanoparticles (**CNPs**, **5*** or **6***) were collected by centrifugation at 4000 rpm for 30 min. The precipitate was stored at 4 °C in sterile Falcon tubes for further studies.

6.1.5. Determination of encapsulation efficiency (EE%). Encapsulation efficiency (EE%) of **CNPs 5*** and **6*** was determined indirectly by quantifying the unencapsulated drug in the supernatant after centrifugation, according to a previously reported method.[61,62] The drug concentration was measured by UV-vis spectrophotometry (T80+ UV/vis, PG Instruments Ltd, UK) (λ_{max} = 283 nm and 305 nm for compounds **5** and **6**, respectively) against the corresponding calibration curves. EE% was calculated as:

$$\mathrm{EE\%} = \frac{W_t\ (\text{total added drug}) - W_s\ (\text{free drug})}{W_t\ (\text{total added drug})} \times 100$$

where W_t is the total drug initially added, and W_s is the drug concentration measured in the supernatant. Full experimental details are provided in the SI. Measurements were performed in triplicate (values are expressed as mean ± SD) and carried out under identical experimental conditions to ensure reliability and reproducibility.

6.1.6. Determination of drug loading percent (DL%). Drug loading (DL%) of **CNPs 5*** and **6*** was determined using a direct quantification method.[62] After separation of the unencapsulated drug by centrifugation, the drug-loaded nanoparticles were lyophilized, dissolved in DMSO, and the drug content was quantified by UV-vis spectrophotometry (T80+ UV/vis, PG Instruments Ltd, UK) against a standard calibration curve. DL% was calculated as:

$$\mathrm{DL\%} = \frac{\text{weight of drug in nanoparticles}}{\text{total weight of nanoparticles}} \times 100$$

where weight of drug in nanoparticles is the actual weight of the drug that was successfully encapsulated, and total weight of nanoparticles includes the weight of encapsulated drug and weight of carrier. The theoretical maximum DL% of 9.09% was calculated from the initial drug-to-chitosan mass ratio of 1 : 10 (w/w), assuming complete incorporation of both components. Measurements were performed in triplicate (values are expressed as mean ± SD) under identical experimental conditions to ensure accuracy and reproducibility. Full experimental details are provided in the SI.

6.1.7. DFT calculations.[63] Gaussian 09 was used to perform DFT calculations for compounds **5** and **6**.[39] The 6-31G(d,p) basis sets and the B3LYP method were used for all calculations. The stability of the optimized compounds was confirmed by the absence of imaginary frequencies.

6.2. Characterization data of products 5 and 6

6.2.1. 4-((1-(Quinolin-3-yl)-1*H*-1,2,3-triazol-4-yl)methoxy) benzaldehyde (5). R_f = 0.3 (*n*-hexane: ethyl acetate, 2 : 1, V/V); m.p: 180–181 °C; IR(KBr) ν_{max} (cm^{-1}): 3138 cm^{-1} (Csp^2-H stretching of triazole ring), 2923 cm^{-1} (CH_2-asymmetric stretching), 2840 cm^{-1} (CH_2-symmetric stretching), 2747 cm^{-1} (Csp^2-H stretching of CHO), 1686 cm^{-1} (C=O stretch), and 1256 cm^{-1} (–OCH_2–). ^{1}H NMR (500 MHz, DMSO-d_6) δ_H: 9.89 (s, 1H, **HC**=O), 9.47 (s, 1H, **Ar-H**), 9.21 (s, 1H, **triazole-H**), 8.96 (s, 1H, **Ar-H**), 8.14 (m, 2H, **Ar-H**), 7.91 (d, J = 7.7 Hz, 2H, **Ar-H**), 7.87 (t, J = 8.4 Hz, 1H), 7.75 (t, J = 7.6 Hz, 1H, **Ar-H**), 7.31 (d, J = 7.6 Hz, 2H), 5.45 (s, 2H, –O**CH_2**–) ppm. ^{13}C NMR (125 MHz, DMSO-d_6) δ_C: 191.5 (**C=O**), 162.9, 147.0, 143.6, 143.3, 131.9, 130.6, 130.1, 130.0, 129.0, 128.7, 128.2, 127.1, 126.3, 123.8, 115.3 (**Ar-C**), 61.4 (–OCH_2–) ppm.

HRMS (ESI) m/z calc. for $C_{19}H_{14}N_4O_2$ $[M + 1]^+$: 331.1195; found 331.1198.

6.2.2 (*E*)-*N*-(4-((1-(quinolin-3-yl)-1*H*-1,2,3-triazol-4-yl) methoxy)benzylidene)-4*H*-1,2,4-triazol-4-amine (6). R_f = 0.4 (*n*-hexane: ethyl acetate,1 : 2, V/V); m.p: 220–221 °C; IR(KBr) ν_{max} (cm^{-1}): 3105 cm^{-1} (Csp^2-H stretching of triazole ring), 2935 cm^{-1} (CH_2-asymmetric stretching), 2851 cm^{-1} (CH_2-symmetric stretching), 1613 cm^{-1} (C=N stretching of imine bond). ^{1}H NMR (500 MHz, DMSO-d_6) δ_H: 9.49 (d, J = 2.8 Hz, 1H, **Ar-H**), 9.21 (s, 1H, C**H**-1,2,3-triazole), 9.18 (s, 2H, C**H**-1,2,4-triazole), 9.03 (s, 1H, **HC**=N), 8.98 (d, J = 2.8 Hz, 1H, **Ar-H**), 8.21–8.09 (m, 2H, **Ar-H**), 7.89 (d, J = 6.8 Hz, 1H, **Ar-H**), 7.86 (d, J = 9.0 Hz, 2H, **Ar-H**), 7.76 (t, J = 7.6 Hz, 1H, **Ar-H**), 7.30 (d, J = 8.8 Hz, 2H, **Ar-H**), 5.42 (s, 2H, –O**CH_2**-) ppm. ^{13}C NMR (125 MHz, DMSO-d_6) δ_C: 161.2 (**C=N**), 157.8, 147.0, 143.7, 143.3, 139, 130.6, 130.4, 130.1, 129.0, 128.7, 128.2, 127.1, 126.2, 125.1, 123.7, 115.5 (**Ar-C**), 61.3 (–OCH_2–) ppm.

HRMS (ESI) m/z calc. for $C_{21}H_{17}N_8O$ $[M + 1]^+$: 397.1525; found 397.1540.

6.3. Biological evaluation

Inhibitory activity against α-amylase[64] and α-glucosidase[65] was assessed according to established protocols, along with evaluation of NO scavenging activity,[66] DPPH radical scavenging activity,[67] and a glucose uptake assay,[68] as detailed in the SI. All

compounds and reference inhibitors were tested at serial dilutions (10–500 μg mL^{-1}). Nanoparticle blank controls were included in all assays to exclude potential interference from the chitosan nanoparticles with absorbance-based readouts. Full methodological details, including enzyme sources, substrate concentrations, pH, incubation conditions, and statistical analysis, are provided in the SI. *In vitro* drug release from **CNPs 5*** and **6*** was evaluated according to a previously reported method using a dialysis bag technique under simulated physiological conditions (phosphate buffer, pH 2.0 and pH 7.4) at 37 ± 0.5 °C over 48 h.[69] The released drug was quantified spectrophotometrically at λ_{max} = 283 nm and 305 nm for compounds **5** and **6**, respectively. Measurements were performed in triplicate (values are expressed as mean ± SD) and carried out under identical experimental conditions to ensure reliability and reproducibility. Full experimental details are provided in the SI.

6.4. *In silico* studies

6.4.1. Molecular docking studies. In addition to the data mentioned in the manuscript, additional information of the molecular docking simulation study is included in the SI.

6.4.2. ADME and drug-likeness analysis. The pharmacokinetic profiles and physicochemical properties of the synthesized compounds **5** and **6** were predicted using the Swiss ADME online tool (https://www.swissadme.ch/).[70] Key ADME descriptors, bioavailability radar, and the boiled-egg Model were computed to assess drug-likeness and medicinal chemistry suitability.

Conflicts of interest

The authors declare no conflicts of interest.

Data availability

All data supporting this study are included in the main article or in the supplementary information (SI). Supplementary information: full spectroscopic characterization of the synthesized compounds ($^1H/^{13}C$ NMR, IR, HRMS), detailed experimental protocols for biological assays, and extended DFT and *in silico* studies data. See DOI: https://doi.org/10.1039/d6ra01266c.

Acknowledgements

The authors sincerely thank Dr P. M. Elhalmoushy, Department of Pharmaceutics & Pharmaceutical Technology, Faculty of Pharmacy, Pharos University in Alexandria, Egypt, for her valuable assistance with the *in vitro* drug release profiles. The authors gratefully acknowledge the Science, Technology & Innovation Funding Authority (STDF), Cairo, Egypt (Project ID: 46267) for supporting this work.

References

1 G. Roglic, *Int. J. Noncommunicable Dis.*, 2016, **1**, 3–8.
2 H. Sun, P. Saeedi, S. Karuranga, M. Pinkepank, K. Ogurtsova, B. B. Duncan, C. Stein, A. Basit, J. C. N. Chan, J. C. Mbanya, M. E. Pavkov, A. Ramachandaran, S. H. Wild, S. James, W. H. Herman, P. Zhang, C. Bommer, S. Kuo, E. J. Boyko and D. J. Magliano, *Diabetes Res. Clin. Pract.*, 2022, **183**, 109119.
3 M. S. Ayoup, A. E. Kassab, A. Sonousi, S. E. Eldaly, J. Y. Al Nawah, H. Abdel-Hamid, D. A. Ghareeb, S. Ashraf and M. A. Fouad, *RSC Adv.*, 2026, **16**, 4170–4183.
4 M. Taha, M. Irshad, S. Imran, S. Chigurupati, M. Selvaraj, F. Rahim, N. H. Ismail, F. Nawaz and K. M. Khan, *Eur. J. Med. Chem.*, 2017, **141**, 530–537.
5 S. Rocha, D. Ribeiro, E. Fernandes and M. Freitas, *Curr. Med. Chem.*, 2020, **27**, 2257–2321.
6 M. M. Rahman, M. R. Islam, F. Rabbi, M. T. Islam, S. Sultana, M. Ahmed, A. Sehgal, S. Singh, N. Sharma and T. Behl, *Curr. Pharm. Des.*, 2022, **28**, 1304–1320.
7 Z. Wang, J. Gao, Y. Zhao, M. Zhou, D. Chen, C. Zhou, S. Yu, Z. Lin, J. Peng, Z. Lin and W. Dai, *LWT*, 2024, **203**, 116392.
8 İ. Çapan, M. Hawash, M. T. Qaoud and N. Jaradat, *ACS Omega*, 2025, **10**, 848–861.
9 A. Amin, T. Qadir, P. K. Sharma, I. Jeelani and H. Abe, *Open Med. Chem. J.*, 2022, **16**, e187410452209010.
10 M. A. Fouad, F. Ferretti, S. Galiè and F. Ragaini, *Eur. J. Org Chem.*, 2023, **26**, e202300809.
11 S. Galiè, M. A. Fouad, C. Abbo, F. Ferretti and F. Ragaini, *Asian J. Org. Chem.*, 2025, **14**, e00555.
12 F. Ragaini, F. Ferretti and M. A. Fouad, *Catalysts*, 2023, **13**, 224.
13 N. Sivaraj, K. Sakthivel, K. Kikushima, M. D. Kostić, T. Dohi and F. V. Singh, *RSC Adv.*, 2025, **15**, 35509–35531.
14 B. Kumaraswamy, K. Hemalatha, R. Pal, G. S. P. Matada, K. R. Hosamani, I. Aayishamma and N. V. S. S. Aishwarya, *Eur. J. Med. Chem.*, 2024, **275**, 116561.
15 R. Neelarapu, J. R. Maignan, C. L. Lichorowic, A. Monastyrskyi, T. S. Mutka, A. N. LaCrue, L. D. Blake, D. Casandra, S. Mashkouri, J. N. Burrows, P. A. Willis, D. E. Kyle and R. Manetsch, *J. Med. Chem.*, 2018, **61**, 1450–1473.
16 G. Ahmad, M. Sohail, M. Bilal, N. Rasool, M. U. Qamar, C. Ciurea, L. G. Marceanu and C. Misarca, *Molecules*, 2024, **29**, 2232.
17 Y. Martynenko, O. Antypenko, I. Nosulenko, G. Berest and S. Kovalenko, *Anti-Inflammatory Anti-Allergy Agents Med. Chem.*, 2020, **19**, 61–73.
18 R. Pal, G. Teli, M. J. Akhtar and G. S. P. Matada, *Eur. J. Med. Chem.*, 2024, **263**, 115927.
19 S. Surapaneni, N. Kerru, R. R. Bhonsle, R. Kapavarapu and S. Maddila, *J. Mol. Struct.*, 2026, **1354**, 144841.
20 S. K. Avula, S. Ullah, S. A. Halim, A. Khan, M. U. Anwar, R. Csuk and A. Al-Harrasi, *J. Mol. Struct.*, 2023, **1274**, 134560.
21 M. Ajmal, A. K. Mahato, M. Khan, S. Rawat, A. Husain, E. B. Almalki, M. A. Alzahrani, A. Haque, M. J. M. Hakme and A. S. Albalawi, *Chem. Biodivers.*, 2024, **21**, e202400637.
22 Q. Guan, S. Xing, L. Wang, J. Zhu, C. Guo, C. Xu, Q. Zhao, Y. Wu, Y. Chen and H. Sun, *J. Med. Chem.*, 2024, **67**, 7788–7824.
23 N. K. Devaraj and M. G. Finn, *Chem. Rev.*, 2021, **121**, 6697–6698.

24 A. L. Harvey, R. Edrada-Ebel and R. J. Quinn, *Nat. Rev. Drug Discovery*, 2015, **14**, 111–129.
25 C. Sanjai, S. L. Gaonkar and S. S. Hakkimane, *ACS Omega*, 2024, **9**, 43302–43318.
26 Y. K. Sung and S. W. Kim, *Biomater. Res.*, 2020, **24**, 12.
27 M. Upadhyay, R. V. Hosur, A. Jha, K. Bharti, P. S. Mali, A. K. Jha, B. Mishra and A. Kumar, *Biomater. Adv.*, 2023, **153**, 213542.
28 R. Weinberg Sibony, O. Segev, S. Dor and I. Raz, *J. Diabetes*, 2024, **16**, e70014.
29 E. O. Yeye, Kanwal, K. Mohammed Khan, S. Chigurupati, A. Wadood, A. Ur Rehman, S. Perveen, M. Kannan Maharajan, S. Shamim, S. Hameed, S. A. Aboaba and M. Taha, *Bioorg. Med. Chem.*, 2020, **28**, 115467.
30 L. Deswal, V. Verma, D. Kumar, C. P. Kaushik, A. Kumar, Y. Deswal and S. Punia, *Arch. Pharm.*, 2020, **353**, e2000090.
31 P. Seboletswe, G. Kumar, L. Kubone, K. Olofinsan, A. Idris, M. S. Islam and P. Singh, *Med. Chem. Res.*, 2024, **33**, 1578–1597.
32 H. Zhai, C. Luo, P. Yang, S. Zhang, H. Wang, Y. Cao, Y. Yang, H. Liu, X. Kong, F. O. Arhema Frejat, C. Ren, X. Shi and C. Wu, *Eur. J. Med. Chem.*, 2022, **238**, 114495.
33 N. C. Silva, C. Chevigny, S. Domenek, G. Almeida, O. B. G. Assis and M. Martelli-Tosi, *Food Chem.*, 2025, **463**, 141129.
34 W. Zhang, in *Nanomaterial: Impacts on Cell Biology and Medicine*, ed. D. G. Capco and Y. Chen, Springer Netherlands, Dordrecht, 2014, DOI: 10.1007/978-94-017-8739-0_2, pp. 19–43.
35 K. Öztürk, M. Kaplan and S. Çalış, *Int. J. Pharm.*, 2024, **666**, 124799.
36 F. T. Jahura, F. K. Ferdousi, A. H. Mostofa Kamal, A. Ul-Hamid, M. Q. Ehsan and M. A. Hossain, *Nanoscale Adv.*, 2025, **7**, 621–633.
37 Y. Herdiana, E. Febrina, S. Nurhasanah, D. Gozali, K. M. Elamin and N. Wathoni, *Pharmaceutics*, 2024, **16**, 1043.
38 V. Butera, *Phys. Chem. Chem. Phys.*, 2024, **26**, 7950–7970.
39 G. W. T. M. J. Frisch, H. B. Schlegel, G. E. Scuseria, J. R. C. M. A. Robb, G. Scalmani, V. Barone, B. Mennucci, H. N. G. A. Petersson, M. Caricato, X. Li, H. P. Hratchian, J. B. A. F. Izmaylov, G. Zheng, J. L. Sonnenberg, M. Hada, K. T. M. Ehara, R. Fukuda, J. Hasegawa, M. Ishida, T. Nakajima, O. K. Y. Honda, H. Nakai, T. Vreven, J. A. Montgomery, Jr, F. O. J. E. Peralta, M. Bearpark, J. J. Heyd, E. Brothers, V. N. S. K. N. Kudin, R. Kobayashi, J. Normand, A. R. K. Raghavachari, J. C. Burant, S. S. Iyengar, J. Tomasi, N. R. M. Cossi, J. M. Millam, M. Klene, J. E. Knox, J. B. Cross, C. A. V. Bakken, J. Jaramillo, R. Gomperts, R. E. Stratmann, A. J. A. O. Yazyev, R. Cammi, C. Pomelli, J. W. Ochterski, K. M. R. L. Martin, V. G. Zakrzewski, G. A. Voth, J. J. D. P. Salvador, S. Dapprich, A. D. Daniels, J. B. F. O. Farkas, J. V. Ortiz, J. Cioslowski, and a. D. J. Fox, *Gaussian 09, Revision A.02*, Gaussian, Inc., Wallingford CT, 2009.
40 K. Tanaka, *Polym. J.*, 2024, **56**, 61–70.
41 C. H. Suresh, G. S. Remya and P. K. Anjalikrishna, *Wiley Interdiscip. Rev. Comput. Mol. Sci.*, 2022, **12**, e1601.
42 A. M. Bayoumy, M. Ibrahim and A. Omar, *Opt. Quant. Electron.*, 2020, **52**, 346.
43 M. S. Altowyan, A. Barakat, A. M. Al-Majid and H. A. Al-Ghulikah, *Molecules*, 2019, **24**, 2342.
44 R. Rafique, K. M. Khan, K. Arshia, S. Chigurupati, A. Wadood, A. U. Rehman, A. Karunanidhi, S. Hameed, M. Taha and M. al-Rashida, *Bioorg. Chem.*, 2020, **94**, 103195.
45 A. Maier, B. Völker, E. Boles and G. F. Fuhrmann, *FEMS Yeast Res.*, 2002, **2**, 539–550.
46 R. Fuhrmeister and J. Streubel, *Bio-protocol*, 2023, **13**, e4733.
47 A. Chattopadhyay, R. Singh, A. K. Das and M. K. Maiti, *Arch. Biochem. Biophys.*, 2020, **695**, 108645.
48 L. F. Bisson, D. M. Coons, A. L. Kruckeberg and D. A. Lewis, *Crit. Rev. Biochem. Mol. Biol.*, 1993, **28**, 259–308.
49 T. Dilip, *Int. J. Eng.*, 2020, **4**, 194–198.
50 S. M. Khirallah, H. M. M. Ramadan, H. A. A. Aladl, N. O. Ayaz, L. A. F. Kurdi, M. Jaremko, S. Z. Alshawwa and E. M. Saied, *Pharmaceuticals*, 2022, **15**, 1576.
51 N. Bouali, M. B. Hammouda, I. Ahmad, S. Ghannay, A. Thouri, A. Dbeibia, H. Patel, W. S. Hamadou, K. Hosni, M. Snoussi, M. Adnan, M. I. Hassan, E. Noumi, K. Aouadi and A. Kadri, *Molecules*, 2022, **27**, 7248.
52 M. C. Tenuta, B. Deguin, M. R. Loizzo, A. Dugay, R. Acquaviva, G. A. Malfa, M. Bonesi, C. Bouzidi and R. Tundis, *Antioxidants*, 2020, **9**, 184.
53 O. A. Saputra, W. N. Safitriono, D. E. K. Maharani, A. Febiana and F. R. Wibowo, *Food Biosci.*, 2023, **53**, 102793.
54 A. Daina, O. Michielin and V. Zoete, *Sci. Rep.*, 2017, **7**, 42717.
55 V. Ivanović, M. Rančić, B. Arsić and A. Pavlović, *Popular Scientific Article*, 2020, **3**, 171–177.
56 A. Daina and V. Zoete, *ChemMedChem*, 2016, **11**, 1117–1121.
57 P. A. Elzahhar, R. Alaaeddine, T. M. Ibrahim, R. Nassra, A. Ismail, B. S. K. Chua, R. L. Frkic, J. B. Bruning, N. Wallner, T. Knape, A. von Knethen, H. Labib, A. F. El-Yazbi and A. S. F. Belal, *Eur. J. Med. Chem.*, 2019, **167**, 562–582.
58 C. B. Pradeep Kumar, B. S. Prathibha, K. N. N. Prasad, M. S. Raghu, M. K. Prashanth, B. K. Jayanna, F. A. Alharthi, S. Chandrasekhar, H. D. Revanasiddappa and K. Yogesh Kumar, *Bioorg. Med. Chem. Lett.*, 2021, **36**, 127810.
59 H. S. Patel and K. B. Patel, *Phosphorus Sulfur Silicon Relat. Elem.*, 2009, **184**, 2443–2452.
60 W. A. Abdelhalim, A. R. Rabee, S. M. Soliman, M. Hagar, E. A. Moneer, B. A. Bakr, A. Barakat, M. Haukka and H. A. Rasheed, *Sci. Rep.*, 2025, **15**, 299.
61 E. Piacentini, in *Encyclopedia of Membranes*, ed. E. Drioli and L. Giorno, Springer Berlin Heidelberg, Berlin, Heidelberg, 2016, DOI: 10.1007/978-3-662-44324-8_1945, pp. 706–707.
62 J. Yan, Z.-Y. Guan, W.-F. Zhu, L.-Y. Zhong, Z.-Q. Qiu, P.-F. Yue, W.-T. Wu, J. Liu and X. Huang, *Pharmaceutics*, 2020, **12**, 216.

63 F. Aytemız, M. Beytur and H. Yuksek, *Eurasia Proceedings of Science, Technology, Engineering & Mathematics*, 2022, **20**, 103–111.
64 V. K. Kumar and K. G. Lalitha, *Indian J. Pharmacol.*, 2014, **46**, 350–351.
65 T. Matsui, C. Yoshimoto, K. Osajima, T. Oki and Y. Osajima, *Biosci., Biotechnol., Biochem.*, 1996, **60**, 2019–2022.
66 E. Mfotie Njoya, A. M. Munvera, P. Mkounga, A. E. Nkengfack and L. J. McGaw, *BMC Complement. Med. Ther.*, 2017, **17**, 199.
67 S. A. Adebayo, M. Ondua, L. Shai and S. Lebelo, *J. Inflamm. Res.*, 2019, 195–203.
68 V. S. Madiwalar, P. S. Dwivedi, A. Patil, S. M. Gaonkar, V. J. Kumbhar, P. Khanal and B. Patil, *J. Diabetes Metab. Disord.*, 2022, **21**, 429–438.
69 S. M. Elkarray, R. M. Farid, M. M. Abd-Alhaseeb, G. A. Omran and D. A. Habib, *J. Drug Deliv. Sci. Technol.*, 2022, **68**, 103086.
70 B. Bakchi, A. D. Krishna, E. Sreecharan, V. B. J. Ganesh, M. Niharika, S. Maharshi, S. B. Puttagunta, D. K. Sigalapalli, R. R. Bhandare and A. B. Shaik, *J. Mol. Struct.*, 2022, **1259**, 132712.